Redox Biology 81 (2025) 103574

Contents lists available at ScienceDirect

Redox Biology

journal homepage: www.elsevier.com/locate/redox

Dual-driven selenium Janus single-atom nanomotors for autonomous regulating mitochondrial oxygen imbalance to catalytic therapy of rheumatoid arthritis

Xu Chen [a,*], Yang Yang [a], Jiajun Chen [c], Yuebing He [a], Yukai Huang [a], Qidang Huang [a], Weiming Deng [a], Ruiqi Zhu [a], Xuechan Huang [a,**], Tianwang Li [a,b,c,***]

[a] Department of Rheumatology and Immunology, Guangdong Second Provincial General Hospital, The Affiliated Guangdong Second Provincial General Hospital of Jinan University, Guangzhou, 510317, PR China
[b] Department of Rheumatology and Immunology, Zhaoqing Central People's Hospital, Zhaoqing, 526000, PR China
[c] The Second School of Clinical Medicine, Southern Medical University, Guangzhou, 510515, PR China

ARTICLE INFO

Keywords:
Selenium nanoparticles
Nanomotor
Nanocatalytic therapy
Oxygen imbalance
Rheumatoid arthritis

ABSTRACT

O_2 deficiency and excessive reactive oxygen and nitrogen species (RONS) in macrophage mitochondria is a key factor causing oxygen imbalance in rheumatoid arthritis microenvironment (RAM). Although nanocatalytic therapy that simultaneously produce O_2 and eliminate RONS offer a novel strategy for RA therapy, the therapeutic efficacy of nanozymes is limited by the lack of autonomous targeting into mitochondria. Herein, we constructed a Janus-structured nanomotor (Pd@MSe) with autonomous targeting ability by embedding Pd single-atom nanozymes into mesoporous selenium (MSe) nanozymes, and obtained a composite nanomotor (Pd@MSe-TPP) with dual-driven forces by modifying with triphenylphosphine (TPP) in MSe hemisphere. In RAM, Pd@MSe-TPP nanomotor achieved autonomously target into macrophages mitochondria with the driven of generation O_2 and TPP targeting effect, moreover under the single-atom effect of the Pd nanozymes enhanced electronic transfer between nanozymes, which significantly boosted GPx catalytic activity further effectively enhanced the diffusion of Pd@MSe-TPP nanomotor, thus quickly resorted the oxygen balance. Additionally, while regulating oxygen imbalance, Pd@MSe-TPP nanomotor enable rapidly blocked the inflammatory cascade, restored mitochondrial function and alleviated inflammation, further prevented cartilage degradation and effectively inhibited RA progression. Therefore, the exquisitely designed nanoplatform to regulation arthritic microenvironment provides a new direction for the RA therapy and the clinical translation of nanomedicine.

1. Introduction

Rheumatoid arthritis (RA) is an autoimmune disease characterized by joint degeneration, with a high disability rate and an incidence rate currently approaching 1 % [1–3]. Although numerous drugs are available for treating RA, the complex pathological mechanism caused by the rheumatoid arthritis microenvironment (RAM) leads to the efficiency of single drug therapy is limited [4–6]. Moreover, this complexity leads to approximately 20 % of cases develop into refractory rheumatoid arthritis [7]. *Douglas J. Veale* and colleagues have further identified the oxygen imbalance within the RAM recently that characterized by the coexistence of hypoxia and excessive reactive oxygen and nitrogen species (RONS) [8]. As the main source of RONS, monocyte-macrophages are prone to mitochondrial dysfunction under inflammatory conditions and lead to hypoxia and production of excessive RONS, which is the main factor of oxygen imbalance in RAM [9,10]. More critically, the progression of oxygen imbalance fosters a self-amplifying loop between hypoxia, excessive RONS, and the inflammatory response, thereby accelerating the advancement of RA. Notably, *Taeghwan Hyeon* and *Huang.ect.* discovered that simultaneously

* Corresponding author.
** Corresponding author.
*** Corresponding author. Department of Rheumatology and Immunology, Guangdong Second Provincial General Hospital, The Affiliated Guangdong Second Provincial General Hospital of Jinan University, Guangzhou, 510317, PR China
E-mail address: 15521370063@163.com (X. Chen).

https://doi.org/10.1016/j.redox.2025.103574
Received 19 November 2024; Received in revised form 20 February 2025; Accepted 26 February 2025
Available online 1 March 2025
2213-2317/© 2025 Published by Elsevier B.V. This is an open access article under the CC BY-NC-ND license (http://creativecommons.org/licenses/by-nc-nd/4.0/).

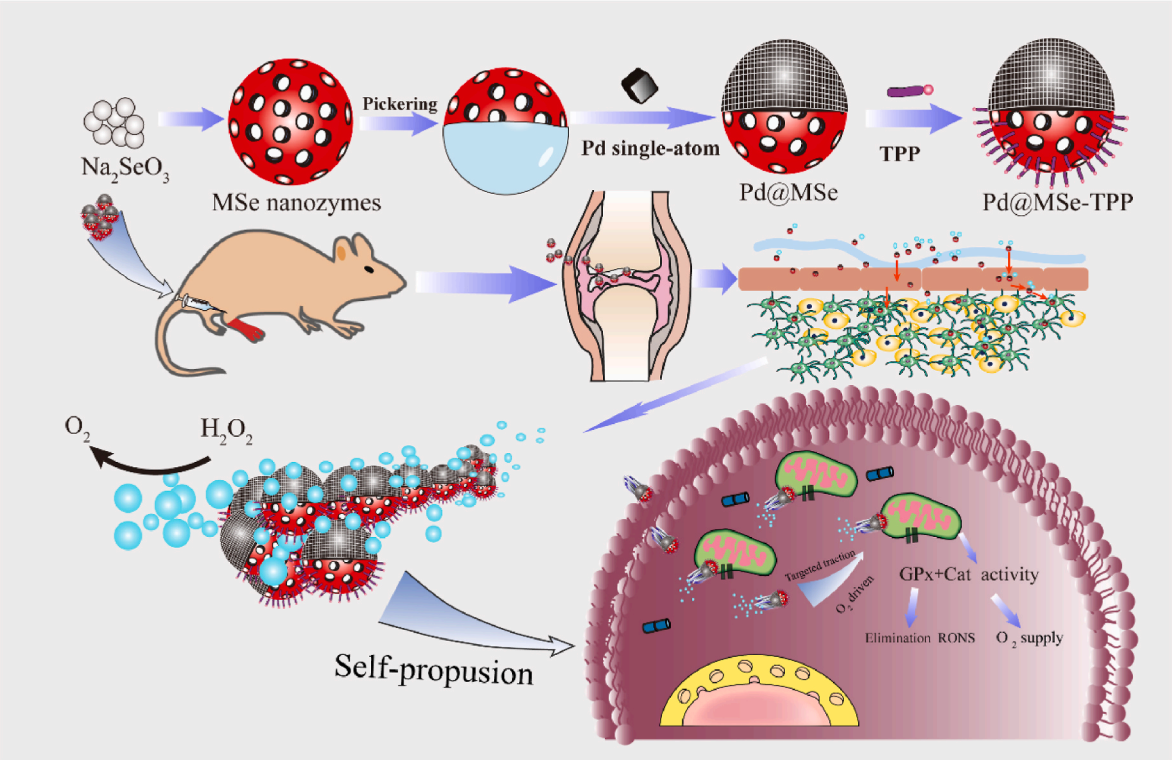

Scheme 1. The illustration of synthesis process of Pd@MSe-TPP nanomotors and its targeted autonomous propulsion and regulation of mitochondrial oxygen imbalance in monocyte-macrophage.

inhibiting the production of RONS and hypoxia within RAM can induce M2 macrophage polarization and enhance the therapeutic efficacy of treating RA [11,12]. Therefore, the concurrent inhibition of excessive RONS and hypoxia in monocyte-macrophage represents an effective strategy for regulating oxygen imbalance and blocking the inflammatory cascade in the treatment of RA.

Nanozymes have demonstrated significant potential in disease therapy through their unique in situ catalytic therapy [13–17,41]. In the context of oxygen regulation, many researchers have developed various metal-based nanozymes aimed at eliminating RONS [18–22]. Additionally, by engineering these nanozymes with modifications have achieved precise regulation of nanozyme activity [23–26]. However, the toxicity and poor metabolism have emerged as significant bottlenecks of metal-based nanozymes limiting the biological application. Selenium (Se), a biocompatible substance and essential element for the human body, not only possesses excellent biocompatibility but also plays a crucial role in maintaining oxidative balance within the body [27–30]. With advancements in nanotechnology, *Chen* [31–33] and our groups [34–36] have constructed various selenium-based therapeutic systems, significantly promoting the research and development of Se-containing substances. Inspired by the catalytic role of Se in selenoenzymes, we have developed a variety of Se-centered nanozymes with glutathione-like catalase activity (GPx) has better stability compared to natural GPx enzymes, and enhanced the antioxidant effect of those nanozymes to treat inflammatory diseases such as RA by modifying the structure and composition [37–40]. However, in RAM, the common feature of Se nanozymes are immobility and nontargeting, as a result, the efficiency of regulating oxygen imbalance is limited due to the Se nanozymes difficulty of actively entering the widely distributed mitochondria. Therefore, a critical challenge that urgently needs to be addressed is how to enhance the autonomous targeting and propulsion capabilities of Se nanozymes to actively and precisely regulate oxygen imbalance within the mitochondria of monocyte-macrophages.

Nanomotors are a class of microscopic machines capable of converting environmental energy into self-propulsion. The self-generated propulsion effectively overcomes biological barriers and enhances active diffusion capabilities [41–43]. Consequently, the autonomous propulsion and diffusion properties of nanomotors provide a valuable strategy for Se nanozymes in precise regulation of oxygen imbalance. Compared to exogenous fuel of nanomotors, the endogenous fuel for autonomous movement is more suited to cellular environments. For example, in tumor and inflammatory microenvironments, based on excessive the RONS in disease microenvironment, researchers have developed various O_2 and NO-driven nanomotors through the reaction between nanoparticles with endogenous RONS [44–49]. Through autonomous propulsion, nanomotors not only enhance the penetration of nanotherapeutic systems in disease microenvironment, but also achieving “one stone two birds” effect by reshaping the disease microenvironment. In addition, researchers have found that nanomotors with asymmetric structures demonstrate stronger propulsion in endogenous fuels. Like *Wilson* designed an asymmetric Pt-based nanomotor capable of catalyzing the production of O_2 from H_2O_2, and found that the asymmetric structure provides enhanced propulsion, which enabling Pt nanomotor directed movement towards neutrophils secreting H_2O_2 without additional H_2O_2 [50]. Therefore, constructing asymmetric nanomotors that utilize excess H_2O_2 as fuel in RAM can generate enhanced propulsion, and incorporating targeted agents to create dual propulsion can be directed nanomotors towards mitochondria. This strategy not only allows for active and precise regulation of oxygen imbalance but also promotes the rapid remodeling of the RAM.

Herein, to develop asymmetric nanomotors for efficient synchronous elimination of hypoxia and RONS in RAM, and as previous reported [38–40], we utilized MSe nanozymes and Pd nanozymes to construct Janus asymmetric nanomotors (Pd@MSe) using Pickering emulsion methods. Under the Cat activity of the Pd single-atom nanozyme, Pd@MSe rapidly catalyzes H_2O_2 to produce O_2, which serves as the driving force to achieve autonomous propulsion. To enable directional autonomous movement into mitochondria of monocyte-macrophages,

we modified the MSe hemisphere with the mitochondria-targeting agent TPP to obtained Pd@MSe-TPP composites nanomotors with dual driving force and targeted autonomous propulsion capabilities. In RAM, Pd@MSe-TPP nanomotors autonomously target and enter the mitochondria of monocyte-macrophages, not only enhancing mitochondrial O_2 generation, but also simultaneously eliminating hypoxia and RONS, thus quickly resorted the oxygen balance. Additionally, while regulating oxygen imbalance, the Pd@MSe-TPP nanomotors rapidly inhibit the inflammatory cascade by upregulating selenoprotein expression, restoring mitochondrial function, alleviating inflammation in RAM, and preventing cartilage degradation, thereby effectively inhibiting the progression of RA (Scheme 1).

2. Materials and method

2.1. Chemicals

L-Cysteine (99 %), (4-Carboxybutyl) triphenylphosphonium bromide (TPP, 98 %), Paraffin liquid (99 %), Sodium tetrachloropalladate (II) (Na_2PdCl_4, 98 %), Polyvinyl Pyrrolidone (PVP, Mw = 2500), Poly (vinyl alcohol) (PVA, Mw = 9000–10000), Polyethylene-polypropylene glycol (F127, Mn = 13000) were purchased from Macklin Regents. Co. China. Sodium selenite (Na_2SeO_3, 99 %), Lipopolysaccharides (LPS, from *Escherichia coli* O55:B5) and other chemicals were purchased from Sigma-Aldrich Chemical. Co. China, which were reagent grade and used without further purification, unless otherwise indicated. Reagent grade water was obtained from a Milli-Q water purification system (Millipore, Bedford, USA). The RAW 264.7, THP-1 and MH7 A cells were obtained from ATCC (Department of Rheumatology and Immunology, Guangdong Second Provincial General Hospital).

2.2. Assessment of human samples

The clinical human samples in this study were authorized by the Research Ethics Committee of Guangdong Second Provincial General Hospital and carried out in compliance with the guidelines outlined in the Declaration of Helsinki (Approval numbers: 2023-KY-KZ-256). Each patient understood the study protocol and signed written consent. The peripheral blood mononuclear cells (PBMCs) were obtained from three RA patients. Control PBMC were obtained from three healthy people. PBMCs were used for transcriptomic analysis to study the oxygen imbalance in RA. Total RNA of the samples was isolated by Trizol reagent (Invitrogen, Carlsbad, CA, United States), and its quantity and purity were analyzed by Bioanalyzer 2100 and RNA 1000 Nano LabChip Kit (Agilent, CA, United States) with a standard of RIN number >7.0, respectively. After the quality check, messenger RNA was purified from total RNA using poly-T oligo-attached magnetic beads according to manufacturer's instructions of Guangzhou Angte Biotech Co.,Ltd (Guangzhou, China). The paired-end sequencing was performed on Illumina Novaseq™ X Plus platform.

2.3. Synthesis of MSe nanozymes

According to our previous reported [38–41], we fore synthesized the aminated mesoporous silica (MSN) as "hard template", then we prepared 5 mL MSN solution (2 mg/mL), and added 5 mg/mL sodium selenite (5 mL) to MSN solution, subsequently added PVA(20 mg) and F127(30 mg) and stirred with for 30 min, the L-cysteine solution (4 mg/mL) was slowly added to the mixture and reaction for 3 h. After completion, the nanoparticles were collected by centrifugation (10000 rpm/min, 20 min), And 200 μL of HF was added to the solution and wash with water three times, finally, the nanoparticles were collected by centrifugation (10000 rpm/min, 20 min) and lyophilized to obtain MSe nanozymes.

2.4. Synthesis of Pd@MSe-TPP nanomotors

Pd@MSe motors were prepared with Pickering emulsions method. Briefly, weigh the MSe nanozymes and disperse them ultrasonically in deionized water. Heat the resulting mixture to 80 °C. Subsequently, incorporate the MSe nanozymes suspension into paraffin liquid at 80 °C, stirring continuously with a magnetic stirrer for 1 h at 80 °C. Upon completion of the reaction, filter out the paraffin liquid-encapsulated MSe nanozymes. Subsequently added PVP (10 mg) and F127(20 mg) mixed with Na_2PdCl_4 (1 mg/mL) and stirred with for 10 min, then the mixture solution was added to the paraffin liquid-encapsulated MSe nanozymes solution and Na_2BH_4 (1 mM, 1 mL) was slowly added to obtain the nanocomposites that Pd nanozymes embed into liquid-encapsulated MSe nanozymes. After centrifugation (10000 rpm/min, 20 min) the precipitation was taken and centrifuged with chloromethane for three times, respectively. The resulting Pd@MSe nanomotors were obtained after dialyze by deionized water for overnight.

Due to there is a mount of –OH groups on the surface of Pd@MSe nanomotors, the carboxylated TPP ((4-Carboxybutyl) triphenylphosphonium bromide) was use the method of esterification reaction to connect with MSe nanozymes, the detail as following: (4-Carboxybutyl) triphenylphosphonium bromide (5 g) dissolved in anhydrous dimethyl sulfoxide (DMSO) (10 mL), then activated with 1-ethyl-3-(3-dimethylaminopropyl)-carbodiimide (EDC, 230 mg) and DMAP (5 mg) for 30 min under nitrogen, then added 2 g Pd@MSe nanomotors and stirred for 12 h in nitrogen to obtain the Pd@MSe-TPP nanomotors. As for carboxylated fluorescein isothiocyanate (FITC) and Cy5 carboxylic acid labeled in MSe nanozymes, the methods were same as before.

2.5. The character of Pd@MSe-TPP nanomotors

The morphology of Pd@MSe-TPP nanomotors was analyzed by a JEM-F200 transmission electron microscope with an acceleration voltage of 200 kV (JEOL, Japan). Element mapping and energy-dispersive X-ray spectroscopy (EDS) were performed using Scanning electron microscopy with ultrahigh resolution cold field emission gun (SEM, Hitachi S-4800, Japan). Single-Atom detection using the scanning transmission electron microscopy (STEM) (FEI Titan Cubed Themis G2 300). The ultraviolet visible-near infrared (UV–Vis–NIR) spectrometer (TU-1810PC, China). The Fourier transform infrared (FT-IR) spectrometer (FTIR-8400S, Tokyo, Japan). XRD was measured on a Rigaku D/MAX-2200 PC XRD system (parameters: Cu Kα, λ = 1.54 A, °40 mA, and 40 kV, D8 DISCOVER, Germany). The N_2 adsorption-desorption isotherm was tested by the Brunauer-Emmett-Teller method to characterize the specific surface area on a Quadraorb Station 4 at 77.3 K (Autosorb-IQ3, USA). XPS was performed on an ESCAlab250 (Thermal Scientific, USA).

2.6. The Cat and GPx activity detection of nanomotors

According to our previous reported [37,38], The standard GR-coupled assay (Beyotime, China) was used to detect the GPx-like activity of nanozymes and nanomotors, the natural GPx as the control. According to the instructions, the same concentration of Pd nanozymes, MSe nanmozymes, Pd@MSe nanomotors, Pd@MSe-TPP nanomotors (40 μg/mL) and GPx (1 U/mL) were mixed with the reaction mixture and incubated for 10 min, respectively. Finally, the mixture solutions were measured the absorbance at 340 nm by automatic microplate reader (Spark 10 M, Tecan, Switzerland).

The standard Catalase test kit (Beyotime, China) was used to measure the Cat-like activity of nanozymes and nanomotors, the natural Cat as the control. According to the instructions, the same concentration of Pd nanozymes, MSe nanmozymes, Pd@MSe nanomotors, Pd@MSe-TPP nanomotors (40 μg/mL) and Cat (1 U/mL) were mixed with the reaction mixture and incubated for 15 min, respectively. Finally, the mixture solutions were measured the absorbance at 520 nm by automatic

microplate reader (NanoD200C, Thermal Scientific, USA).

Then, the H_2O_2 concentration in after reaction and cells was measured with a H_2O_2 assay kit (Beyotime, China). And the O_2 concentration generation in solution after relation with Pd nanozymes, MSe nanmozymes, Pd@MSe nanomotors, Pd@MSe-TPP nanomotors (40 μg/mL) using a dissolved oxygen meter oxygen probe (JPBJ-608 portable, China).

2.7. The movement recording and analysis of nanomotors

A confocal laser scanning microscope (CLSM 800, ZEISS, Germany) with a high-speed camera (sCMOS) was used to record the motion behavior of MSe nanozymes, Pd@MSe nanomotors and Pd@MSe-TPP nanomotors. The motion trajectories of the MSe nanozymes, Pd@MSe nanomotors and Pd@MSe-TPP nanomotors (40 μg/mL) under different H_2O_2 concentrations (0.5, 1, 2, 4, 8 and 16 mM for PBS and cell suspension for different density cells) were recorded. The motion was recorded for 15 s and at least 10 nanomotors were analyzed under each condition. Subsequently, the tracking image sequences and the speed of the nanomotors were analyzed by ImageJ plugin manual tracking according to the previous reports. Mean-square-displacement (MSD) analysis trough the self-diffusiophoretic model of Golestanian et al. [23].

2.8. The cellular uptake and penetration detection of nanomotors

RAW 264.7 cells (1×10^5) were inoculated into the glass bottom cell culture plates (20 mm, NEST). After adherence the LPS (100 ng/mL) was added to activate RAW 264.7 cells. The activated for 1 h, 20 μL of Cy5-labeled MSe nanozymes, Pd@MSe nanomotors and Pd@MSe-TPP nanomotors (40 μg/mL) were added and co-incubated for 6 h, respectively. Then washed three times with PBS and stained with DAPI and DIO for 30 min, the fluorescence in cells were measured by confocal laser scanning microscope (CLSM 800, ZEISS, Germany). In addition, the protocol of mitochondrial colocalization similar to the detection of cellular uptake.

Then the penetration performance of Cy5-labeled MSe nanozymes, Pd@MSe nanomotors and Pd@MSe-TPP nanomotors (40 μg/mL) were further tested by cultivating the cell spheres. The activated RAW 264.7 cells (1×10^3) were inoculated into the 24 ultra-low adhesion pore plates (Corning, USA). After 7 days the cells become cell spheres, 20 μL of Cy5-labeled MSe nanozymes, Pd@MSe nanomotors and Pd@MSe-TPP nanomotors (40 μg/mL) were added and co-incubated for 6 h, respectively. Then washed three times with PBS and stained with DAPI for 20 min, the fluorescence in cells were measured by confocal laser scanning microscope with Z-axis scanning (CLSM 800, ZEISS, Germany).

2.9. The detection of intracellular ROS

RAW 264.7 cells (1×10^5) were seeded onto 6-well plates, after adherence the cells were co-incubated with Pd nanozymes, MSe nanmozymes, Pd@MSe nanomotors, Pd@MSe-TPP nanomotors (40 μg/mL) for 6 h, respectively, then washed with PBS and added LPS (100 ng/mL) activated 1 h. Subsequently, the cells were cultured for another 6 h in hypoxia (2 % O_2) environment, in addition, the non-activated cells without treatment were also cultured in hypoxia (2 % O_2) environment or normoxic (21 % O_2) for 6 h. After incubation, the cells were washed three times with PBS and stained with ROS probe (2,7-Dichlorodihydrofluorescein diacetate (DCFH-DA)) for 30 min and measured by fluorescence microscopy (Axio Observer 3, ZEISS, Germany) with the excitation wavelength at 495 nm and an emission peak at 525 nm.

2.10. The detection of intracellular oxygen imbalance

The O_2 generation efficiency in RAW 264.7 cells by O_2 sensing probe ([(Ru(dpp)$_3$)] Cl_2 (Sigma-Aldrich, USA)). RAW 264.7 cells (1×10^5) were seeded onto 6-well plates, after adherence the cells were co-incubated with Pd nanozymes, MSe nanmozymes, Pd@MSe nanomotors, Pd@MSe-TPP nanomotors (40 μg/mL) for 6 h, respectively, then washed with PBS and added LPS (100 ng/mL) activated 1 h. Subsequently, the cells were cultured for another 6 h in hypoxia (2 % O_2) environment, in addition, the non-activated cells without treatment were also cultured in hypoxia (2 % O_2) environment or normoxic (21 % O_2) for 6 h. Then, the cells were incubated with O_2 sensing probe (Ex = 488 nm, Em = 620 nm) for another 4 h and then observed by fluorescence microscopy (Axio Observer 3, ZEISS, Germany).

2.11. The detection of pro-inflammatory cytokines in vitro

The RAW 264.7 cells with a density of 1×10^5 cells per well were seeded onto 6-well plates, after adherence the cells were exposed to the mediums containing Pd nanozymes, MSe nanmozymes, Pd@MSe nanomotors, Pd@MSe-TPP nanomotors (40 μg/mL) for 6 h, respectively, then washed with PBS and added LPS (100 ng/mL) activated 1 h. Subsequently, the cells were cultured for another 6 h in hypoxia (2 % O_2) environment, in addition, the non-activated cells without treatment as control group were cultured in normoxia (21 % O_2). After incubation, then extracted the and centrifugal collection of cell culture medium, the typical inflammatory cytokines (TNF-α (Tumor necrosis factor-α), interleukin-6 (IL-6) and interleukin-1β (IL-1β) were detected by ELISA (4A Biotech, China).

2.12. The immunostaining of hypoxia and mitochondrial function

The detection of hypoxia and mitochondrial function by immunostaining. The RAW 264.7 cells and THP-1 cells were seeds in the glass bottom cell culture plates and after treatments with above experiments, each group of cells was washed three times with PBS. The cells were then fixed with 4 % paraformaldehyde for 20 min and washed with PBS. Subsequently, 1 % Triton X-100 was applied for 15 min. Following this, the cells were blocked with 5 % BSA for 2 h. After washing with PBS, the RAW 264.7 cells were incubated with hypoxia-inducible factor-1(HIF-1α, bs-0737R, IF = 1:100, Bioss, China), cyclic GMP–AMP synthase (cGAS, bs-9537R, WB = 1:100–500, Bioss, China), stimulator of interferon genes (STING, bs-8335R, IF = 1:50–200, Bioss, China) or C–C Chemokine receptor 2B (CCR2 antibodies, bsm-62473R, WB = 1:1000–2000,IF = 1:100–500, Bioss, China) overnight, respectively, then stained with Alexa Fluor 488-labeled secondary antibody or Cy 5-labeled secondary antibody (Bioss, China) and DAPI (Beyotime, China). The THP-1 cells were incubated with cGAS, STING, CCR2 antibodies, Recombinant Human Translocase Of Outer Mitochondrial Membrane 20 (TOM 20, #42406, IF = 1:100–400,CST,USA), Transcription Factor A (TFAM, #42406, IF = 1:100–200,CST,USA) or 8-hydroxy-2′-deoxyguanosine (8-oHdG, bs-1278R, IF = 1:500, Bioss, China) overnight, respectively, then stained with Alexa Fluor 488-labeled secondary antibody or Cy 5-labeled secondary antibody (Bioss, China) and DAPI (Beyotime, China). Finally, the cells were observed with confocal laser scanning microscope (CLSM 800, ZEISS, Germany).

2.13. The western blotting analysis

The proteins expression in RAW 264.7 cells above groups also tested with western blotting (WB), after treatments, the cells were lysed in 200 μL of PBS with proteinase inhibitor cocktail and collected the proteins by centrifugation. After measurement of protein concentration by BCA assay (Beyotime, China) the proteins were mixed with loading buffer and boiled at 95 °C for 10 min for denaturation, and loaded on sodium dodecyl sulfate polyacrylamide gel. After 50 min of electrophoresis at 110 V, proteins were transferred to nitrocellulose membrane (BioRad) using a Trans-Blot SD wet electrophoretic transfer cell (Bio Rad) for 70 min at 120 V. To avoid non-specific binding, membranes were then blocked with 5 % BSA for 2 h. Next, membranes were probed with primary antibodies; HIF-1α(bs-0737R, WB = 1:1500–2000, Bioss,

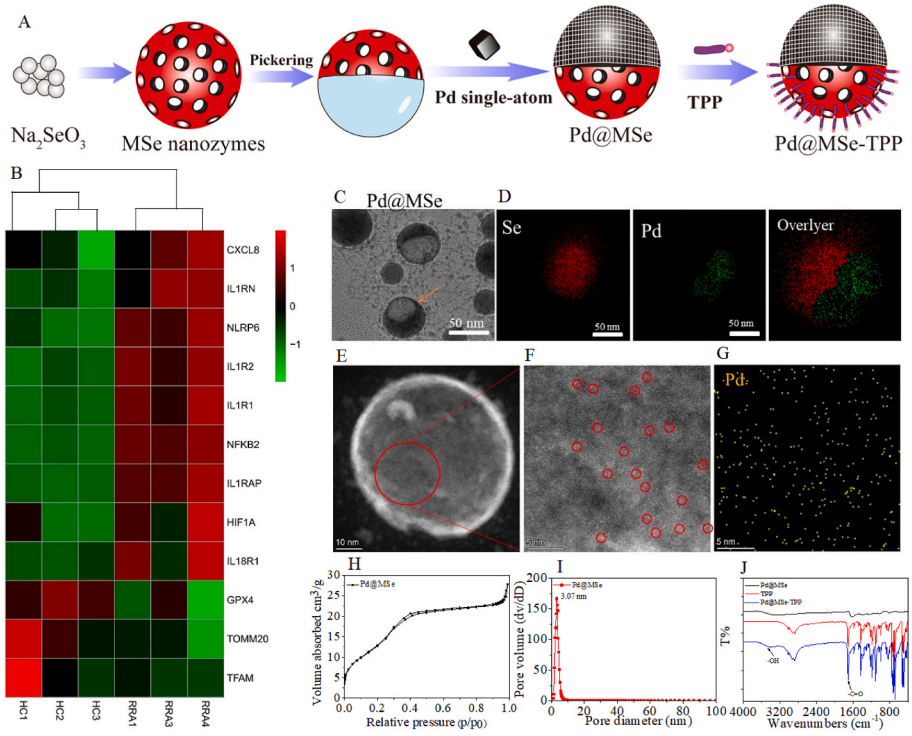

Fig. 1. Oxygen imbalance detection in RAM and Fabrication of Pd@MSe-TPP nanomotors. (A) The illustration of synthesis steps of Pd@MSe-TPP nanomotors. (B) The gene heatmap (fold change >2 and P < 0.05) of healthy individuals and RA patients related genes in PBMC. For each group, n = 3 biological replications. (C) The TEM image of Pd@MSe nanomotors. Scale bar = 50 nm. (D) Element mapping of the Pd@MSe nanomotors. Scale bars: 50 nm. (E) HAADF-STEM image of atomic arrangement at the Pd@MSe nanomotors nanolayer. (F) High-resolution HAADF-STEM image of the amorphous Pd@MSe nanomotors nanolayer; the Pd atoms are marked by red circles. (G) The element mapping of Pd atoms in Pd@MSe nanolayer by STEM. (H) Nitrogen adsorption desorption isotherms for Pd@MSe nanomotors. (I) The pore size distributions of Pd@MSe nanomotors derived from desorption isotherm measurements testing with BJH methods. (J) The FTIR spectrum of TPP, Pd@MSe and Pd@MSe-TPP nanomotors.

China), Glutathione peroxidase 4(GPx4, bs-3884R, WB = 1:500–2000, Bioss, China), Tumor necrosis factor-α (TNF-a, bs-2081R, WB = 1:500–2000, Bioss, China), Phospho–NF–kappaB p65 (Ser536) (Pp65 (NF-κB), #3033, WB = 1:1000, CST, USA), CCR2 (bsm-62473R, WB = 1:1000–2000,Bioss, China), TFAM (#42406, WB = 1:1000, CST, USA) overnight at 4 °C. The next day, membranes were washed with TBST three times and reacted with HRP-conjugated secondary antibodies for 1 h. After washing, membranes were then developed using chemiluminescence detection system (Fluor Chem R).

2.14. Animals and animal models

C57BL/6 mice (male, 7–8 weeks) were purchased from the Guangdong Medical Experimental Animal Center and DBA/1 (male, 8–9 weeks) were purchased from the Guangdong GemPharmatech Co., Ltd. The Animal care was in accordance with the institutional guidelines and approved by the Animal Care and Use Committee of Guangdong Second Provincial General Hospital (Approval number:2023-DW-KZ-100-02).

Collagen-induced arthritis (CIA) model was established by injecting 100 μL of emulsified solution (1:1) mixing type 2 collagen (2 mg/mL) and complete Freund's Adjuvant (CFA) (1 mg/mL) into C57BL/6 mice and DBA/1 mice at the base of the tails, and injecting another 100 μL of emulsified solution (1:1) mixing type 2 collagen (2 mg/mL) and CFA (1 mg/mL) into the tails at 21 days later intradermally. The healthy mice were applied as the normal control groups.

2.15. Biodistribution analysis of nanomotors

The CIA models C57BL/6 mice were randomly assigned with 3 groups (n = 3), then the Cy5 labeled MSe nanozymes, Pd@MSe nanomotors and Pd@MSe-TPP nanomotors with were intratracheally administration. Then fluorescence was detected at 0, 1, 2 h, respectively by Maestro in vivo optical imaging system (Cambridge Research and Instrumentation, Inc.). After 2 h, the mice were euthanized and extract the joints for immunofluorescence analysis to observe the distribution of MSe nanozymes, Pd@MSe nanomotors and Pd@MSe-TPP nanomotors within the joints by fluorescence microscopy (Axio imager A2, ZEISS, Germany).

2.16. The therapy of CIA model mice

The male DBA/1 CIA model mice were randomly divided into five groups (5 mice in each group) and treated on day 1 with PBS, Pd nanozymes, MSe nanozymes, Pd@MSe nanomotors, and Pd@MSe-TPP nanomotors (1 mg/kg), respectively. Additionally, normal mice were used as a control group. During treatments, all the mice of treatments groups were received injections every three days, and the changes in weight and joint diameter of each mouse were measured. And the thickness of each limb of mice were also measured to further evaluate the joint swelling degree. Arthritis scores of each limb of mice were obtained from day 1 according to the selling degree, following the standard evaluation process [21]. The joint was rated as 0 if there was no sign of erythema or swelling; 1 if the joint had any erythema or mild swelling; 2 if erythema and mild swelling extended from the ankle to the tarsus; 3 if erythema and moderate swelling extended from the ankle joint to the metatarsal joint; 4 if the joint had erythema and severe swelling including ankles, paws, and stiffness of fingers or limbs. Clinical scores for four limbs were summed up for a mouse to have an overall arthritis severity score, with a higher score indicating more severe arthritis.

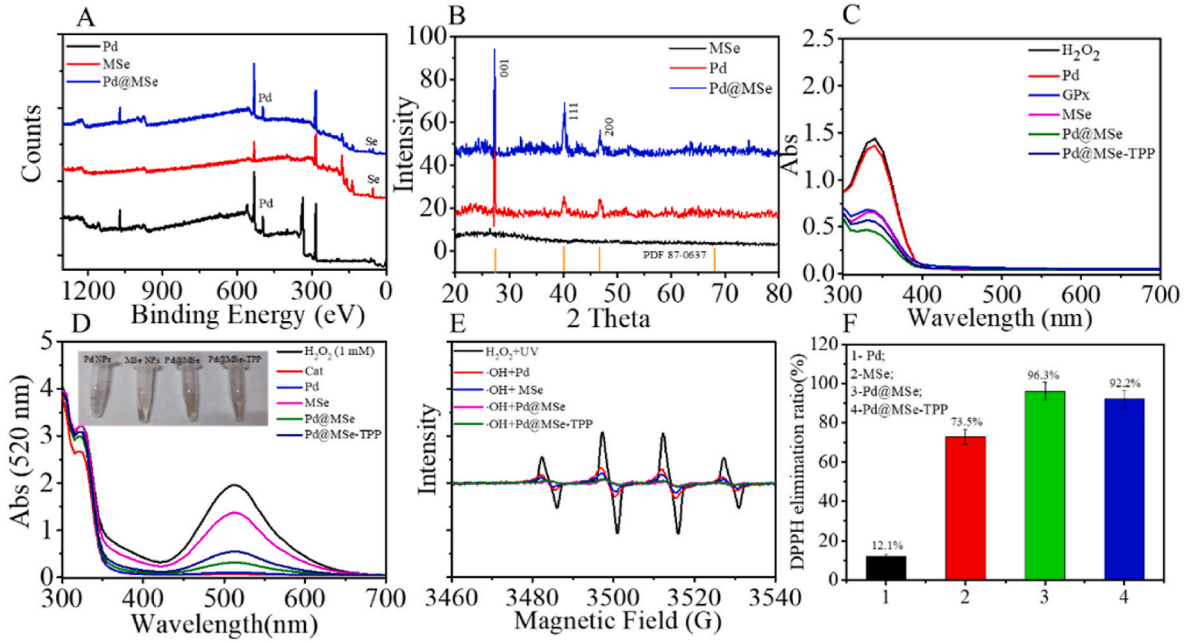

Fig. 2. The conformation and enzyme-like activity of Pd@MSe-TPP nanomotors. (A) The XPS spectrum of Pd, MSe and Pd@MSe nanomotors. (B) The XRD patterns of Pd, MSe and Pd@MSe nanomotors (The Standard PDF card of PD was: JCPDS NO.87-0637). (C) The GPx-like activity of Pd, GPx, MSe, Pd@MSe and Pd@MSe-TPP nanomotors, respectively. (D) The Cat-like activity of Pd, Cat, MSe, Pd@MSe and Pd@MSe-TPP nanomotors, respectively. (E) The ERP spectra of detecting ·OH elimination in an aqueous solution of Pd, MSe, Pd@MSe and Pd@MSe-TPP nanomotors after reaction with H_2O_2 under irradiation with UV. (F) The RNS scavenging activity of Pd, MSe, Pd@MSe and Pd@MSe-TPP nanomotors detecting with DPPH, (n = 3, mean = ±SD).

2.17. The inflammation and micro-CT detection of CIA model mice

To evaluate the severity of RA and bone damage, we detected the cytokines in serum by ELISA and the morphology of bones by micro-CT. Firstly, the whole blood was collected by the eyeballs, and then clotted at room temperature for 30 min to obtained the serum samples, subsequently, the serum samples were centrifuged at 4000×*g* for 20 min to collect the supernatant. And the supernatants were immediately measured using the TNF-*α*, IL-6 and IL-1βELISA kits (4A Biotech, China).

Then the four limbs of mice sacrificed at day 30 were fixed in 10 % buffered formalin, after three days taken the hind leg bones and scanned at 70 kV and 100 μA with the resolution of 20 μm in micro-CT (Sky-Scan1276) for 30 min. Then, the dataset was reconstructed using ZKKS-Micro CT 4.1 workplace to obtain the 3D images of joints and to measure the ratio between bone surface and bone volume (BS/TV).

2.18. The pathological analysis by pathological sections

After therapy, the four limbs were collected after mice were euthanized, and the hind knee joints of all groups were constructed to pathological sections that stained with H&E, immunohistochemistry (CCR2), immunofluorescence (HIF-α) and Safranin O-Fast Green. The image was obtained by fluorescence microscopy (Axio imager A2, ZEISS, Germany).

Statistical analysis: All data were expressed as mean result ± standard deviation (SD) based on at least three independent experiments. A p-value <0.05 was considered statistically significant. Statistical analyses were conducted by Origin 8.5 using the One Sample T-tests for experiments with multiple groups, while a two-tailed, unpaired *t*-test was used for data with two groups.

3. Results and discussion

3.1. The oxygen imbalance detection in RAM and Fabrication of Pd@MSe-TPP nanomotors

In order to validate the presence of oxygen imbalance in RAM and to justify the design of our Pd@MSe-TPP nanomotors, we performed a transcriptomic analysis comparing the RNA expression profiles in PBMCs, which include monocytes and lymphocytes, from three healthy individuals and three RA patients. As shown in Fig. 1A, RA patients showed elevated levels of inflammatory cytokines such as interleukin-8 (CXCL8), interleukin-1(IL-1), NOD-like receptor family pyrin domain containing 6(NLRP6), and NF-κB, along with a widespread increase in HIF expression. In contrast, the expression levels of antioxidant-related genes, including GPx4, TOMM20, and TFAM, were lower than those observed in healthy individuals. These findings suggested that mitochondrial function is compromised that is an oxygen imbalanced state in the PBMCs of RA patients.

Based on our previous reported [38–40], we developed nanomotors composed of Pd nanozymes like-Cat activity and MSe nanozymes like-GPx activity to simultaneously eliminate RONS and address O_2 insufficiency, thereby improving the oxygen imbalance in RAM. After synthesizing the Pd@MSe nanomotors, compared with the seed liquid of $PdCl_2$, Pd@MSe nanomotors is darker in color, and the spectrum of UV–vis is also changed, which showed a wide acromion at 260–270 nm (Figure s1). The structure of the Pd@MSe nanomotors is shown in Fig. 1B, TEM images revealed spherical nanoparticles approximately 60 nm with typical Janus structures. The elements mapping images identified that the asymmetrically distributed elements were primarily Se and Pd (Fig. 1C). EDS analysis further showed that the Se content was 30.7 % and the Pd content was 4.8 % (Figure s2), confirming the successful synthesis of Janus asymmetric Pd@MSe nanomotors. Additionally, the TEM images showed the Pd nanozymes with ultra-small size (Figure s3), to verify the structure of the Pd nanozymes in Pd@MSe nanomotors, the AC-HAADF-STEM revealed isolated bright spots (marked with red circles) within the Pd@MSe structure (Fig. 1D–E). EDS

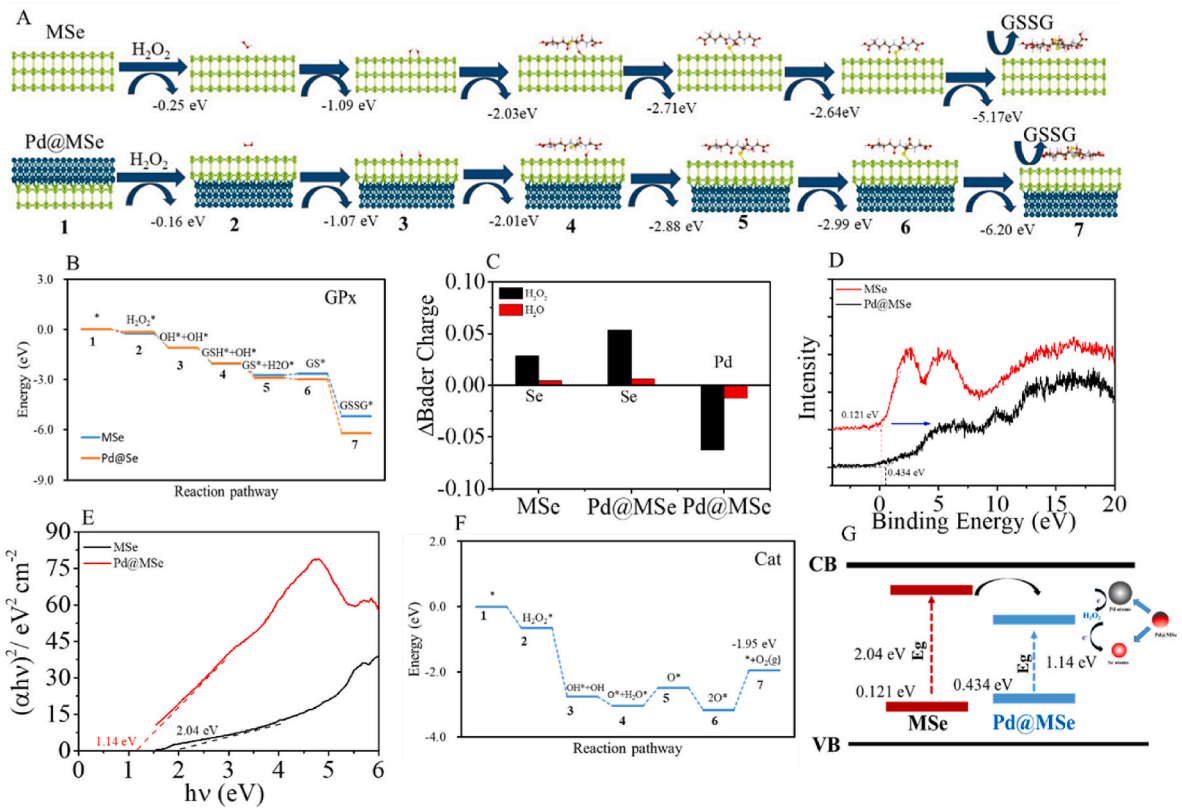

Fig. 3. Theoretical calculation of catalytic GPx-like pathways of Pd@MSe nanomotors. (A) Schematic diagrams of the catalytic of GPx-like pathways corresponding to MSe nanozymes and Pd@MSe nanomotors. (B) Free energy profiles for H_2O_2 reaction through GPx-like pathways on MSe nanozymes and Pd@MSe nanomotors. (C) Bader charge difference between the adsorption structures of H_2O_2 and H_2O in Pd@MSe nanomotors, the positive represents electron injection, while the negative represents electron depletion. (D) The VB of MSe nanozymes and Pd@MSe nanomotors. (E) The Eg of MSe nanozymes and Pd@MSe nanomotors. (F) Free energy profiles for H_2O_2 reaction through Cat-like pathways on MSe nanozymes and Pd@MSe nanomotors. (G) The illustration of electron transfer and energy band change during electron transition in Pd@MSe nanomotors.

elemental mapping indicated that these bright spots corresponded to Pd (Fig. 1F), confirming that the Pd nanozymes are in a single-atom state. Nitrogen adsorption-desorption analysis demonstrated that Pd@MSe is a mesoporous structure (Fig. 1G) with a pore size of 3.07 nm (Fig. 1H), providing a foundation for generating stronger propulsion. To enhance the autonomous propulsion and mitochondrial targeting of the Pd@MSe nanomotors, we attached the mitochondria-targeting agent carboxylated TPP to the MSe hemisphere through ester bonds. Fourier Transform infrared spectroscopy (FT-IR) of the TPP-functionalized Pd@MSe-TPP nanomotors showed that the infrared absorption peaks of Pd@MSe were retained, along with the characteristic absorption peaks of TPP, including the –C═O characteristic peak at 1650 cm^{-1} ~1690 cm^{-1}, indicating that TPP was successfully connected via ester bonds (Fig. 1I). This confirms the successful synthesis of Janus-structured Pd@MSe-TPP nanomotors.

3.2. *The conformation and enzyme-like activity of Pd@MSe-TPP nanomotors*

Due to the enzymatic activity of nanozymes is closely related to their phase composition, we first analyzed the conformation of Pd@MSe-TPP nanomotors. As shown in Fig. 2A, X-ray photoelectron spectroscopy (XPS) analysis revealed the presence of both Pd and Se in Pd@MSe structure. High-solution XPS spectra of Se(3d) and Pd(3d) further showed the valent is 0 that in Pd@MSe nanomotors, and due to the low content of Pd resulted in a significantly lower absorption intensity compared to MSe, which corroborated the results of TEM (Figure s4A-D). X-ray diffraction (XRD) analysis showed the MSe is an amorphous nanoparticle that consistent with previous reports that red nano-selenium is an amorphous nanoparticle. However, with the incorporation of Pd nanocrystalline, the XRD patterns of Pd@MSe display a crystal structure and similar to that of the Pd nanozymes (PDF#87–0637), mainly exposed the (001), (111), and (200) crystal planes (Fig. 2B). Furthermore, the crystal structure of Pd@MSe nanomotors was confirmed by HRTEM. The results of SAED further showed the exposing planes mainly are (111) and (200) and interplanar spacing is 0.22 nm of Pd@MSe nanomotors in identified crystalline regions (Figure s5A), which also consistent with the Pd nanozymes (Figure s5B).

Based on the phase structure of the Pd@MSe nanomotors, we further evaluate the enzymatic activity of both Pd@MSe and the TPP-functionalized Pd@MSe-TPP nanomotors. Initially, we assessed the GPx-like activity of the individual components within the Pd@MSe-TPP nanomotors. As shown in Fig. 2C, the Pd nanozymes did not exhibit any GPx-like activity, whereas MSe nanozymes retained the high GPx activity. Similar Pd@MSe and Pd@MSe-TPP nanomotors display strong GPx-like activity, and it is interestingly that Pd@MSe and Pd@MSe-TPP nanomotors exhibited higher activity GPx than MSe nanozymes with the same concentration. Kinetic analysis revealed that the maximum reaction rate (Vmax) of Pd@MSe was 1.2 times that of MSe, with the Michaelis constant (Km) only 0.8 times that of MSe (Figure s6A). Subsequently, we measured the Cat-like activity of Pd, MSe, Pd@MSe, and Pd@MSe-TPP nanomotors. As illustrated in Fig. 2D, Pd, Pd@MSe, and Pd@MSe-TPP nanomotors all enable to produce O_2 when mixed with H_2O_2, demonstrating they showed significant Cat-like activity. And the enzyme kinetics detection showed that Vmax of Pd nanozymes was 4.87 mM/min and Km was 0.7253 mM/L, while Vmax of Pd@MSe reached 3.69 mM/min and Km was 1.03047 mM/L (Figure s6B). Due to Se nanozymes inherently possess the ability to directly scavenge RONS, we

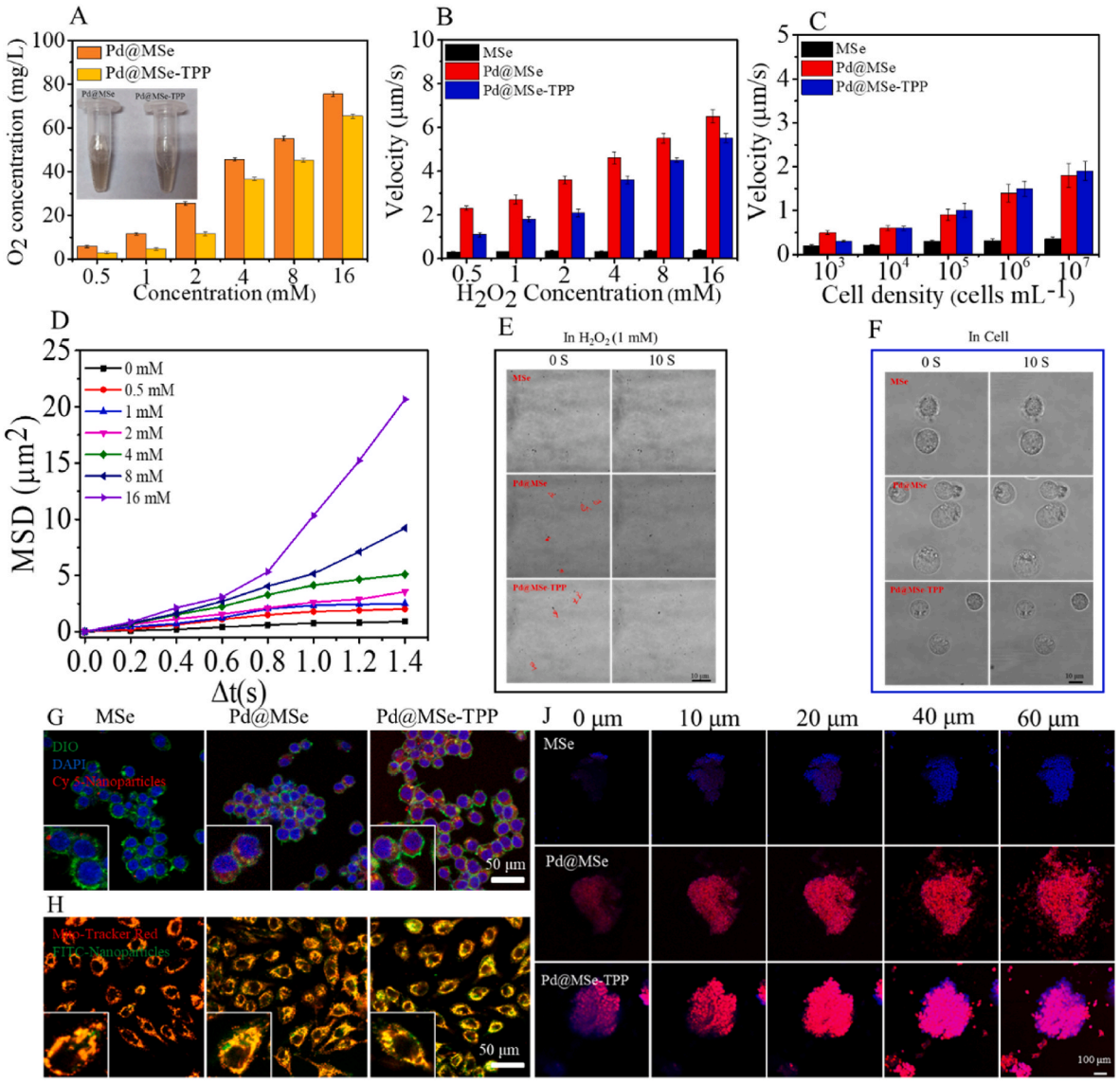

Fig. 4. The self-propelled targeting motion of Pd@MSe-TPP nanomotors. (A) The O_2 generation in different concentration of H_2O_2 aqueous solution under the catalysis of Pd@MSe and Pd@MSe-TPP nanomotors. (B) The Velocity of MSe nanozymes, Pd@MSe and Pd@MSe-TPP nanomotors presented in cell fluid containing different concentration of H_2O_2. (C) The velocity of Pd@MSe and Pd@MSe-TPP nanomotors after reaction with different concentration of H_2O_2 aqueous solution. (D) The MSD curve of Pd@MSe-TPP nanomotors in different concentration of H_2O_2 aqueous solution. (E) The motion trajectory of MSe nanozymes, Pd@MSe and Pd@MSe-TPP nanomotors in H_2O_2 (1 mM) aqueous solution. (F) The motion trajectory of MSe nanozymes, Pd@MSe and Pd@MSe-TPP nanomotors in RAW 264.7 cells. (G) The cellular uptake of MSe nanozymes, Pd@MSe and Pd@MSe-TPP nanomotors incubated with RAW 264.7 cells for 6 h, respectively. (H) The targeted mitochondrial detection of MSe nanozymes, Pd@MSe and Pd@MSe-TPP nanomotors incubated with RAW 264.7 cells for 6 h, respectively (Scale bar = 100 μm). (J) The penetration depth of MSe nanozymes, Pd@MSe and Pd@MSe-TPP nanomotors in RAW 264.7 3D cell spheres (Scale bar = 100 μm, n = 3, mean ± SD).

further investigated the efficiency of Pd, MSe, Pd@MSe, and Pd@MSe-TPP nanomotors in scavenging RONS. Liquid FT-IR revealed significant changes in the 2800 cm^{-1}–3000 cm^{-1} for MSe and Pd@MSe nanomotors before and after reacting with H_2O_2, further confirming that both MSe and Pd@MSe nanomotors can react with H_2O_2 (Figure s7A). Electron Paramagnetic Resonance (ESR) analysis further showed that the produced ·OH with UV-irradiated H_2O_2, which were significantly reduced in the presence of Pd, MSe, Pd@MSe, and Pd@MSe-TPP nanomotors, respectively (Fig. 2E). According to the standard curve for H_2O_2 concentration (Figure s7B), the ·OH scavenging efficiencies of Pd, MSe, Pd@MSe, and Pd@MSe-TPP nanomotors were quantitatively calculated to be 70.1 %, 79.7 %, 94.3 %, and 90.8 %, respectively (Figure s7C), Pd@MSe and Pd@MSe-TPP nanomotors further showed a concentration-dependent effect (Figure s7D). However, when assessing the efficiency of Pd, MSe, Pd@MSe, and Pd@MSe-TPP nanomotors in scavenging RNS using the 1,1-diphenyl-2-picrylhydrazyl (DPPH), we found that the inhibition trends were similar to their GPx-like activity. Pd nanozymes exhibited very weak RNS scavenging efficiency. Consequently, the RNS scavenging efficiency of MSe reached 73.5 %, while the incorporation of Pd nanozymes in Pd@MSe and Pd@MSe-TPP nanomotors further increased this efficiency to 96.3 % and 92.2 %, respectively. Thus, those results demonstrate that constructing Janus-structured Pd@MSe-TPP nanomotors not only endowed MSe with autonomous targeted driving ability but also significantly enhanced its reactive activity.

3.3. *Theoretical calculation of catalytic pathways of Pd@MSe nanomotors*

In above experiments, Pd@MSe nanomotors exhibited higher GPx

activity compared to MSe nanozymes. To elucidate the mechanisms and the differences between the catalytic activity Pd@MSe nanomotors and MSe nanozymes, we conducted systematic density functional theory (DFT) calculations to simulate the catalytic GPx-like pathways of both MSe nanozymes and Pd@MSe nanomotors in their reactions with H_2O_2. According to the reaction pathways, the overall GPx-like process by which MSe and Pd@MSe eliminate H_2O_2 proceeds as follows:

$$H_2O_2 + 2\,\mathrm{GSH} \xrightarrow{G} GSSG + 2H_2O.$$

Therefore, under the catalytic action of GPx, H_2O_2 reacts with two molecules of GSH, yielding one molecule of GSSG and two molecules of H_2O. DFT simulations further revealed that the reaction sites for the substrates during those catalytic reactions are primarily concentrated in the surface Se atomic layer with seven steps (Fig. 3A). The analysis of the key intermediates and Gibbs free energy (ΔG) along the reaction pathways of MSe and Pd@MSe indicated that differences between them begin to emerge at the fifth step in adsorbing the GS*and H_2O*. At this stage, Pd@MSe nanomotors exhibit a lower ΔG during adsorption, and the ΔG for GSSG* adsorption in the seventh step being −6.02 eV, which lower than that for MSe (Fig. 3B). These results suggest that the Pd@MSe nanomotors with higher GPx-like activity is due to lower energy barrier in the catalytic process. Bader charge analysis also confirmed the previous results, the detection showed that during the reaction process, Pd atoms lose electrons while Se atoms gain electrons, and there are more electrons being gained by Se in Pd@MSe nanomotors, thus the abundant electron flows out from Pd sites injects into Se sites, leading to a higher GPx-like activity of Pd@MSe nanomotors (Fig. 3C). Valence band (VB) detection further showed that the transfer of Pd electrons to Se results in an elevated valence band in Pd@MSe nanomotors. Compared to MSe, the VB increased from 0.121 eV to 0.434 eV (Fig. 3D). Furthermore, the incorporation of Pd nanozymes in Pd@MSe nanomotors also narrowed the energy band gap (Eg), the Eg of Pd@MSe nanomotors decreased by 0.9 eV compared to MSe nanozymes (Fig. 3E), thereby facilitating easier electron transitions and conferring higher GPx-like activity in Pd@MSe nanomotors. Additionally, we utilized DFT to simulate the reaction process of Pd@MSe nanomotors with H_2O_2 through Cat-like activity. The detailed reaction pathway indicates that the process of Pd@MSe nanomotors adsorbing H_2O_2 and subsequently desorbing to produce O_2 is also divided into six steps (Figure s8), and the ΔG for the O_2 generation is only −1.95 eV, which suggests that the catalysis of H_2O_2 to produce O_2 by Pd@MSe nanomotors is an efficient and spontaneous process. Therefore, with the incorporation of single-atom Pd nanozymes into Pd@MSe nanomotors, the electron density and electron transfer efficiency in MSe nanozymes are enhanced (Fig. 3G), which not only effectively enhances the GPx-like activity of MSe, but also improves the overall reactivity of Pd@MSe nanomotors.

3.4. The self-propelled targeting motion of Pd@MSe-TPP nanomotors

After confirming the Cat-like activities of Pd@MSe and Pd@MSe-TPP nanomotors, we systematically explored the autonomous movement of Pd@MSe and Pd@MSe-TPP nanomotors in aqueous solutions and in monocyte-macrophage systems. We first examined the O_2 generation capacity of Pd@MSe and Pd@MSe-TPP nanomotors in different concentrations of H_2O_2 aqueous solutions. As shown in Fig. 4A, due to the strong Cat activity of Pd@MSe and Pd@MSe-TPP nanomotors, bubble formation was observed even at concentration of 500 μM, and the generation of O_2 after reaction with Pd@MSe and Pd@MSe-TPP nanomotors reached 5.86 mg/L and 2.35 mg/mL, respectively, showing a concentration-dependent behavior. Then we used the RAW 264.7 cell model to measure the H_2O_2 concentration in the culture medium and within the cells after LPS activation. The results indicated a significant increase in H_2O_2 concentration in RAW 264.7 cells following LPS activation, which increased further with cell density, reaching 301 μM at a density of 10^7 cells (Figure s9). Next, we recorded the movement of MSe nanozymes, Pd@MSe, and Pd@MSe-TPP nanomotors using LSCM and analyzed their trajectories with Image J. In aqueous solutions with varying concentrations of H_2O_2, MSe nanozymes exhibited only low-speed Brownian motion due to the lack of autonomous propulsion. In contrast, Pd@MSe and Pd@MSe-TPP nanomotors displayed autonomous movement driven by O_2, with significantly increased movement speed in a concentration-dependent manner. In 1 mM H_2O_2 solution, the self-propelled movement speeds of Pd@MSe and Pd@MSe-TPP nanomotors reached 2.7 μm/s and 1.8 μm/s, respectively (Fig. 4B). The corresponding images and videos further corroborated the movement speed of Pd@MSe is faster can be attributed to its stronger catalase activity (Fig. 4E–s10, Movie 1-9). The mean square displacements (MSDs) of Pd@MSe-TPP nanomotors, calculated according to Golestanian et al.'s self-diffusiophoretic model [51], further demonstrated that the MSDs of Pd@MSe-TPP nanomotors increased with higher fuel concentrations (Fig. 4D). This enhanced motion behavior is expected to greatly improve the diffusion efficiency in the H_2O_2-rich of RAM.

We then observed and analyzed the movement of MSe nanozymes, Pd@MSe, and Pd@MSe-TPP nanomotors under cellular conditions. Before examining their intracellular movement, we assessed the cytotoxic effects of the components in Pd@MSe-TPP nanomotors. RAW 264.7 and MH7A cells were incubated with varying concentrations of Pd nanozymes, MSe nanozymes, Pd@MSe, and Pd@MSe-TPP nanomotors for 24 h. It was found that MSe nanozymes, Pd@MSe and Pd@MSe-TPP nanomotors showed good biocompatibility even at 160 μg/mL (Figure s11A-B). There are also showing no significant hemolytic activity in MSe nanozymes, Pd@MSe and Pd@MSe-TPP nanomotors after co-incubation with red blood cells (Figure s11C). Subsequently, we introduced MSe nanozymes, Pd@MSe, and Pd@MSe-TPP nanomotors into LPS-activated RAW 264.7 cell suspensions at different densities. The results were similar to those observed in the H_2O_2 solution. MSe nanozymes exhibited only slight Brownian motion, while Pd@MSe and Pd@MSe-TPP nanomotors exhibited clear autonomous diffusion movement, with movement speed increasing with cell density. At $1*10^7$ cells density, due to the increased H_2O_2 concentration in the cell suspension, the movement speeds of Pd@MSe and Pd@MSe-TPP nanomotors reached 1.8 μm/s and 1.9 μm/s, respectively (Fig. 4C). The observation of movement images and videos of MSe nanozymes, Pd@MSe, and Pd@MSe-TPP nanomotors within RAW 264.7 cells further confirmed that Pd@MSe and Pd@MSe-TPP nanomotors generate propulsion to achieve autonomous diffusion movement within cells. The autonomous movement of Pd@MSe-TPP nanomotors was more pronounced under the driven by O_2 and the targeting agent (Fig. 4F–Movie 10-12). Subsequently, we evaluated the targeting functionality of Pd@MSe-TPP nanomotors through cellular uptake and mitochondrial co-localization experiments. After co-incubating with RAW 264.7 cells for 6 h, we observed that mitochondria are widely distributed in cells. In addition, Pd@MSe-TPP nanomotors exhibited significantly better cellular uptake compared to MSe nanozymes and Pd@MSe nanomotors, particularly in their autonomous diffusion targeting mitochondria (Fig. 4G). Additionally, a greater number of Pd@MSe-TPP nanomotors entered the mitochondria with (Fig. 4H). Under dual propulsion, Pd@MSe-TPP nanomotors also demonstrated enhanced motility and penetration in 3D spheroids of RAW 264.7 cells, with a penetration depth nearly 20 μm greater than that of Pd@MSe nanomotors (Fig. 4J). Collectively, these findings suggest that dual-powered Pd@MSe-TPP nanomotors provide a promising therapeutic strategy for modulating mitochondrial dynamics within monocyte-macrophage cells.

3.5. The activity of Pd@MSe-TPP nanomotors targeted regulate oxygen imbalance

Monocyte-macrophage dysfunction in mitochondrial function plays a crucial role in the development of RONS imbalance and the progression of RA [52,53]. Therefore, regulating the mitochondrial oxygen imbalance to restore their function is a key step in addressing ROS

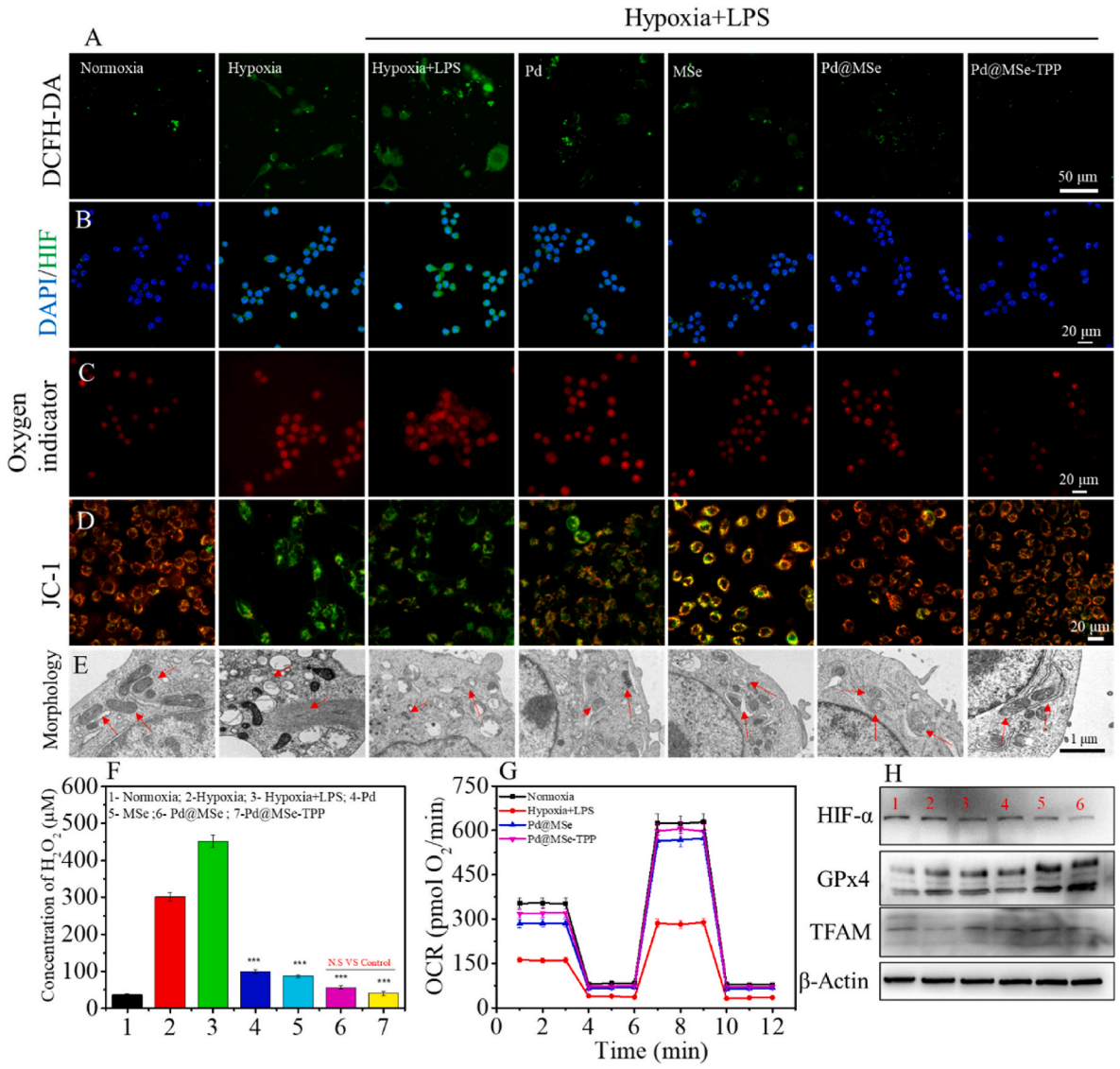

Fig. 5. Targeted regulation of mitochondrial oxygen imbalance in monocyte-macrophages. (A) The ROS level in RAW264.7 cells probed by DCFH-DA after various treatments. (B) The hypoxic level in RAW264.7 cells by immunofluorescence after various treatments. (C) The O_2 level in RAW264.7 cells by O_2 indicator ([(Ru(dpp)$_3$)] Cl_2) after various treatments. (D) The mitochondrial membrane potential of RAW264.7 cells by JC-1 after various treatments. (E) The mitochondrial morphology of RAW264.7 cells by JC-1 after various treatments. (F) The H_2O_2 concentration in RAW264.7 cells after various treatments. (G) The measurement of mitochondrial OCR in RAW 264.7 cells after various treatments, (n = 3, mean ± SD, *p < 0.05, **p < 0.01, ***p < 0.001). (H) Western blotting for HIF-α,GPx 4 and TFAM proteins in RAW264.7 cells after various treatments(1 = Normoxia; 2 = Hypoxia + LPS; 3 = Pd; 4 = MSe; 5 = Pd@MSe; 6 = Pd@MSe-TPP).

imbalance. Based on this, RAW 264.7 cells and human monocytes THP-1 were used as research models. To further activate the monocyte-macrophage and enhance the diffusion of Pd@MSe-TPP nanomotors, a cell density of 1 × 10^5 cells and 250 μM H_2O_2 were used as additional activators and fuel in the following experiments. During the simultaneous elimination of ROS and hypoxia, we first assessed the activity of Pd@MSe-TPP nanomotors in ROS elimination. As shown in Fig. 5A, fluorescence detection using the ROS probe DCFH-DA revealed low fluorescence intensity under normoxic conditions, indicating low ROS levels in non-activated RAW 264.7 cells. However, under hypoxic conditions or the hypoxia combination with LPS (100 mg/mL) condition, the intracellular ROS concentration sharply increased, consistent with our previous transcriptomic analysis results. Subsequently, under hypoxic conditions with LPS, we pre-incubated the cells with Pd nanozymes, MSe nanozymes, Pd@MSe, and Pd@MSe-TPP nanomotors. The results showed that all of these had ROS-eliminating activity. Specifically, Pd nanozymes decomposed H_2O_2 to produce O_2 through Cat activity, inhibiting the generation of •OH, while MSe nanozymes effectively suppressed ROS through GPx activity. The findings further demonstrated that Pd@MSe and Pd@MSe-TPP nanomotors had enhanced ROS elimination efficiency due to the autonomous motion. The Pd@MSe-TPP nanomotors, with their targeted autonomous motion, exhibited a better ROS elimination. Quantitative analysis revealed that the intracellular H_2O_2 concentration after treatment with Pd@MSe-TPP nanomotors was only 40.4 μM, close to the normal cellular level of 36.5 μM (Fig. 5F). Immunofluorescence detection of HIF-α clearly showed that under hypoxic conditions and LPS stimulation, HIF-α levels in RAW 264.7 cells rapidly increased, but after ROS elimination by Pd nanozymes, MSe nanozymes, Pd@MSe, and Pd@MSe-TPP nanomotors, HIF-α levels were also suppressed, exhibiting the same trend (Fig. 5B). Correspondingly, following the alleviation of hypoxia in RAW 264.7 cells, fluorescence signals from the [Ru(dpp)$_3$]Cl_2 probe indicated a reduction in fluorescence after treatment with Pd nanozymes, MSe nanozymes, Pd@MSe, and Pd@MSe-TPP nanomotors, suggesting an improvement in intracellular O_2 levels. Notably, the O_2 supply in cells treated with Pd@MSe-TPP nanomotors approached

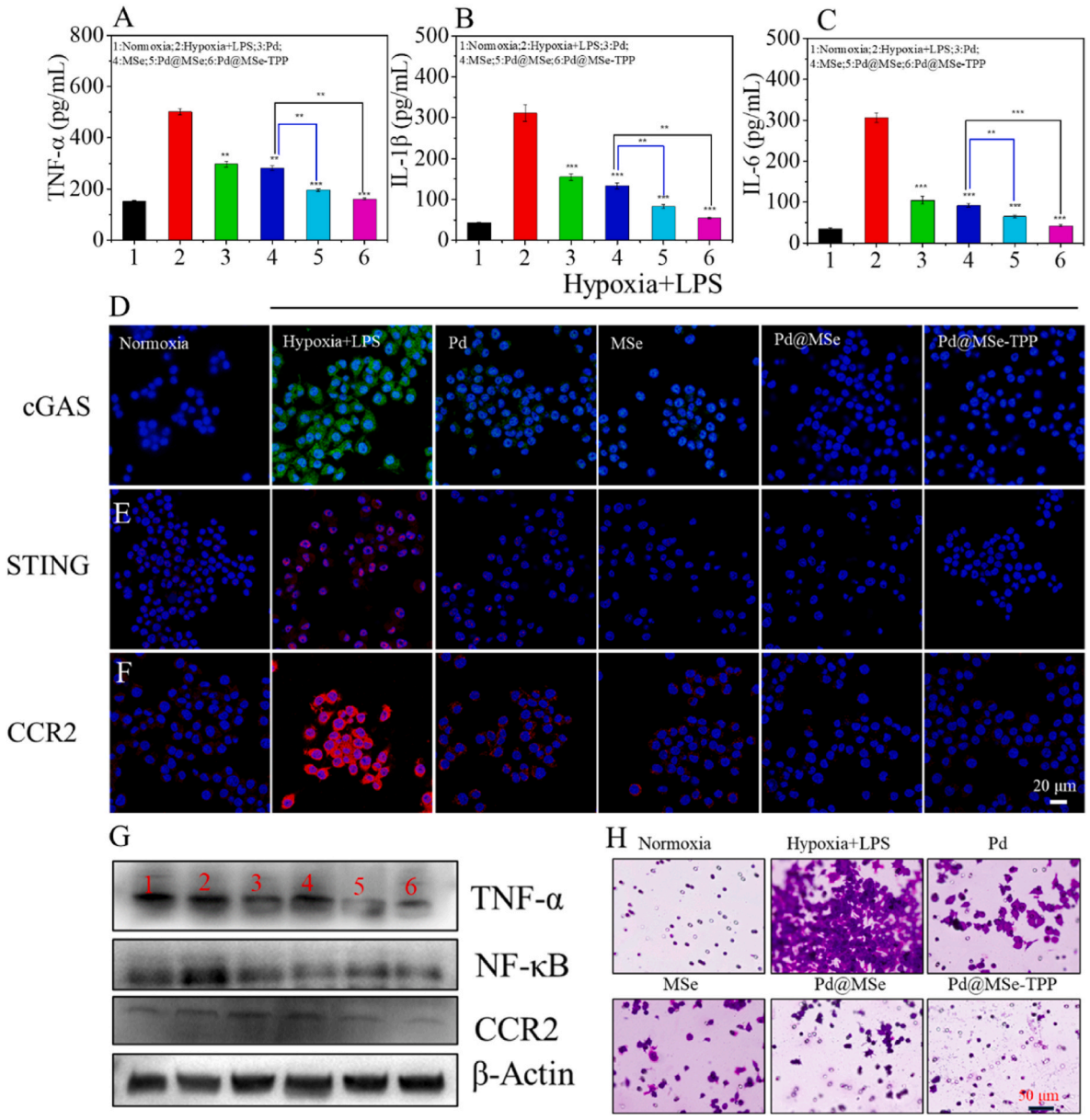

Fig. 6. Targeted inhibited inflammatory response in monocyte-macrophages. (A–C) The levels of pro-inflammatory cytokines (TNF-α, IL-1β and IL-6) by ELISA in cells supernatant after various treatments. (D–E) The expression of cGAS-STING and CCR2 in RAW 264.7 cells by immunofluorescence after various treatments. (G) Western blotting for TNF-α, NF-κB and CCR2 in RAW 264.7 cells after various treatments(1 = Normoxia; 2 = Hypoxia + LPS; 3 = Pd; 4 = MSe; 5 = Pd@MSe; 6 = Pd@MSe-TPP). (H) The images of the chemotactic effect of RAW 264.7 cells stained with crystal violet staining in Transwell system after various treatments, (n = 3, mean ± SD, *p < 0.05, **p < 0.01, ***p < 0.001).

normal levels (Fig. 5C). This demonstrates that the catalytic therapy with Pd@MSe-TPP nanomotors achieved efficient and simultaneous elimination of ROS and hypoxia in inflammatory monocyte-macrophages, thereby improving oxygen imbalance.

After regulating the oxygen imbalance, we proceeded to assess the changes in mitochondrial function in inflammatory monocyte-macrophages. First, JC-1 staining revealed that under hypoxia and combined hypoxia with LPS stimulation, JC-1 predominantly existed in the monomer form in RAW 264.7 cells. This indicates that the mitochondrial membrane potential in RAW 264.7 cells significantly decreased under inflammatory conditions (Fig. 5D). Moreover, the cell morphology underwent noticeable changes that RAW 264.7 cells exhibited inflammatory polarization with more filopodia under combined hypoxia and LPS stimulation. However, after treatment with Pd nanozymes, MSe nanozymes, Pd@MSe, and Pd@MSe-TPP nanomotors provided significant protection to the mitochondria. The levels of JC-1 monomers decreased, and the levels of JC-1 aggregates increased. Notably, under the therapy of Pd@MSe-TPP nanomotors, there was almost no decrease in mitochondrial membrane potential in RAW 264.7 cells, and the mitochondria remained undamaged. Consequently, the cell morphology was relatively intact, and the level of inflammatory polarization was low (Figure s12). Subsequent analyses of mitochondrial lesions and mitochondrial respiratory capacity in RAW 264.7 cells further validated these findings. Compared to the intact mitochondria observed in normal cells, mitochondrial swelling, fragmentation, disruption of membrane integrity, and damaged or absent cristae were observed under the combined stimulation of hypoxia and LPS (Fig. 5E). Moreover, with the mitochondrial damage, its respiratory function is also seriously affected, which can be clearly observed by mitochondrial oxygen consumption ratio (OCR), the overall mitochondrial respiratory capacity of RAW 264.7 cells in effect of hypoxia and LPS was inhibited (Fig. 5G). However, with treatments of Pd@MSe-TPP nanomotors, the

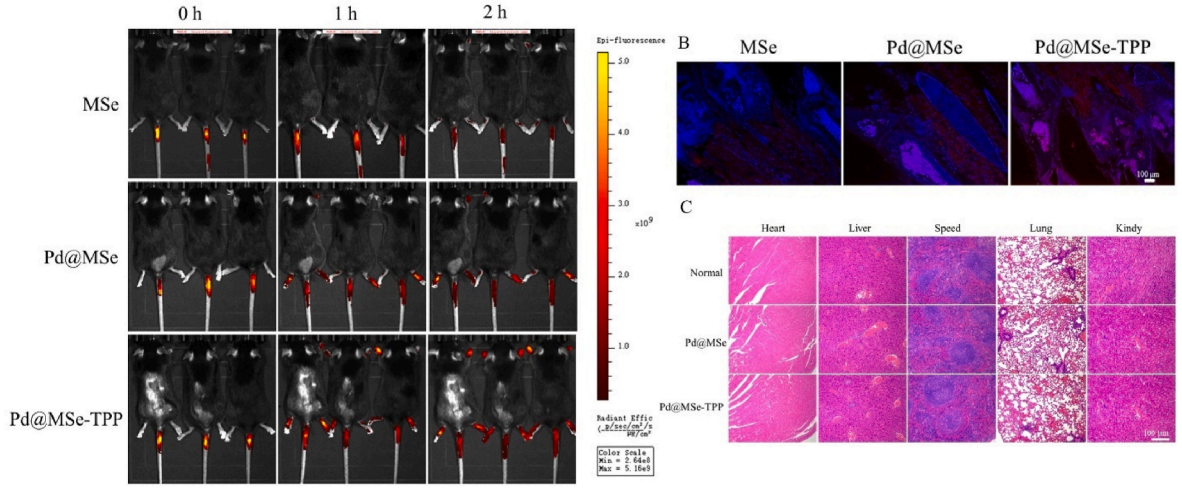

Fig. 7. In vivo imaging and distribution of Pd@MSe-TPP nanomotors in CIA model. (A) The bioluminescence images in the CIA mice after treated with MSe nanozymes, Pd@MSe nanomotors, and Pd@MSe-TPP nanomotors at 0,1 h and 2 h. (B) The distribution of MSe nanozymes, Pd@MSe nanomotors, and Pd@MSe-TPP nanomotors in CIA mice joints through the fluorescent section. (C) Histological sections of major organs extracted 24 h after treatment Pd@MSe nanomotors and Pd@MSe-TPP nanomotors. Images were acquired at 200 × magnification, (n = 3, mean ± SD).

synchronous inhibition of ROS and hypoxia effectively prevented mitochondrial damage. Furthermore, WB analysis showed that Pd@MSe-TPP nanomotors inhibited HIF-α expression in RAW 264.7 cells and protected mitochondria from RONS damage by increasing the levels of GPx4 and TFAM (Fig. 5H). Similarly, in THP-1 cells, the same trend was observed. Following the improvement of oxygen imbalance by Pd@MSe-TPP nanomotors, the levels of TFAM and the human-specific antibody TOM20 were effectively increased, while the expression of the human-specific marker 8-OHdG was inhibited, indicating a similar restoration of mitochondrial dysfunction. Therefore, based on the above experiments and previous reports, we infer that the autonomous targeted diffusion of Pd@MSe-TPP nanomotors effectively enhanced their catalytic therapeutic efficiency within cellular mitochondria, improved the oxygen imbalance in inflammatory monocyte-macrophages, and protected mitochondria from inflammatory damage by elevating the levels of selenoproteins and other antioxidant proteins. This study demonstrates the potential of constructing nanomotors to enhance the antioxidative and anti-inflammatory levels of MSe nanozymes within inflammatory monocytes.

3.6. *The activity of Pd@MSe-TPP nanomotors targeted inhibited inflammatory response*

Based on the excellent performance of Pd@MSe-TPP nanomotors in modulating mitochondrial oxygen imbalance in monocytes-macrophage cells, we subsequently assessed the inflammatory response within these cells after the correction of oxygen imbalance. First, we measured the levels of three pro-inflammatory factors (TNF-α, IL-1β and IL-6) in the culture medium of each group. The results indicated these pro-inflammatory factors showed a rapid increase in RAW 264.7 cells under the combined effect of hypoxia and LPS, which is indicative of a severe inflammatory response. However, treatment with Pd nanozymes, MSe nanozymes, Pd@MSe, and Pd@MSe-TPP nanomotors led to varying degrees of reduction in these factors, showing a trend consistent with the regulation of oxygen imbalance. This suggests that Pd@MSe-TPP nanomotors effectively suppressed the inflammatory response by modulating mitochondrial oxygen imbalance within RAW 264.7 cells (Fig. 6A–C).

We further examined the changes in immune responses associated with inflammation following the application of Pd nanozymes, MSe nanozymes, Pd@MSe, and Pd@MSe-TPP nanomotors, to elucidate their role in blocking the inflammatory cascade. The cGAS-STING pathway is an intrinsic factor and signaling pathway responsible for inflammation triggered by mitochondrial dysfunction [54], while CCR2, a key receptor for chemokines, plays a significant role in the development and spread of the inflammatory response and the infiltration of inflammatory cells in mononuclear-macrophages [55]. NF-κB, a nuclear transcription factor, acts as a switch in regulating inflammation and plays a crucial role in the initiation and progression of the inflammatory response [56]. Therefore, we primarily assessed cGAS-STING, CCR2 and NF-κB to demonstrate their blockade in the inflammatory cascade. Immunofluorescence analysis of cGAS-STING (Fig. 6D and E) and CCR2 (Fig. 6F) revealed a significant increase in their expression in RAW 264.7 cells under the combined influence of hypoxia and LPS. This indicates the cGAS-STING pathway is activated with the inflammatory response increasing, and with the expression of CCR2 increasing further promoted the inflammatory response overflow. Due to the varying degrees of protection offered by Pd nanozymes, MSe nanozymes, Pd@MSe, and Pd@MSe-TPP nanomotors, the expression of cGAS-STING and CCR2 was inhibited to different extents. Among them, Pd@MSe-TPP nanomotors exhibited the strongest protective effect due to their autonomous targeting motion, resulting in the best inhibition of cGAS-STING and CCR2, approaching normal cell levels. Then we further found that Pd nanozymes, MSe nanozymes, Pd@MSe, and Pd@MSe-TPP nanomotors produced similar therapeutic effects in human mononuclear-macrophage THP-1 cells, with Pd@MSe-TPP nanomotors almost completely suppressing the expression of cGAS-STING and CCR2 (Figure s14). Subsequently, we further detected the expression of related proteins in RAW 264.7 cells by WB, the WB results showed that compared with the group of Hypoxia + LPS, treatment with Pd@MSe and Pd@MSe-TPP nanomotors not only inhibited the expression of NF-κB and CCR2 but also suppressed the expression of the pro-inflammatory factor TNF-α within cells (Fig. 6G). Additionally, using the Transwell co-culture system, we observed that the migration and infiltration of macrophages were significantly inhibited following treatment with Pd@MSe-TPP nanomotors, further corroborating the aforementioned results (Fig. 6H). After 24 h of co-incubation, only 26 RAW 264.7 cells had migrated to the lower layer, a number close to that of the normal cell group (Figure s15). Therefore, these experiments demonstrate that Pd@MSe-TPP nanomotors, by effectively modulating mitochondrial oxygen imbalance in mononuclear-macrophages, not only rapidly suppress the inflammatory response within cells but also effectively inhibit the inflammatory cascade by blocking key factors at various stages of the inflammatory process, thereby preventing further

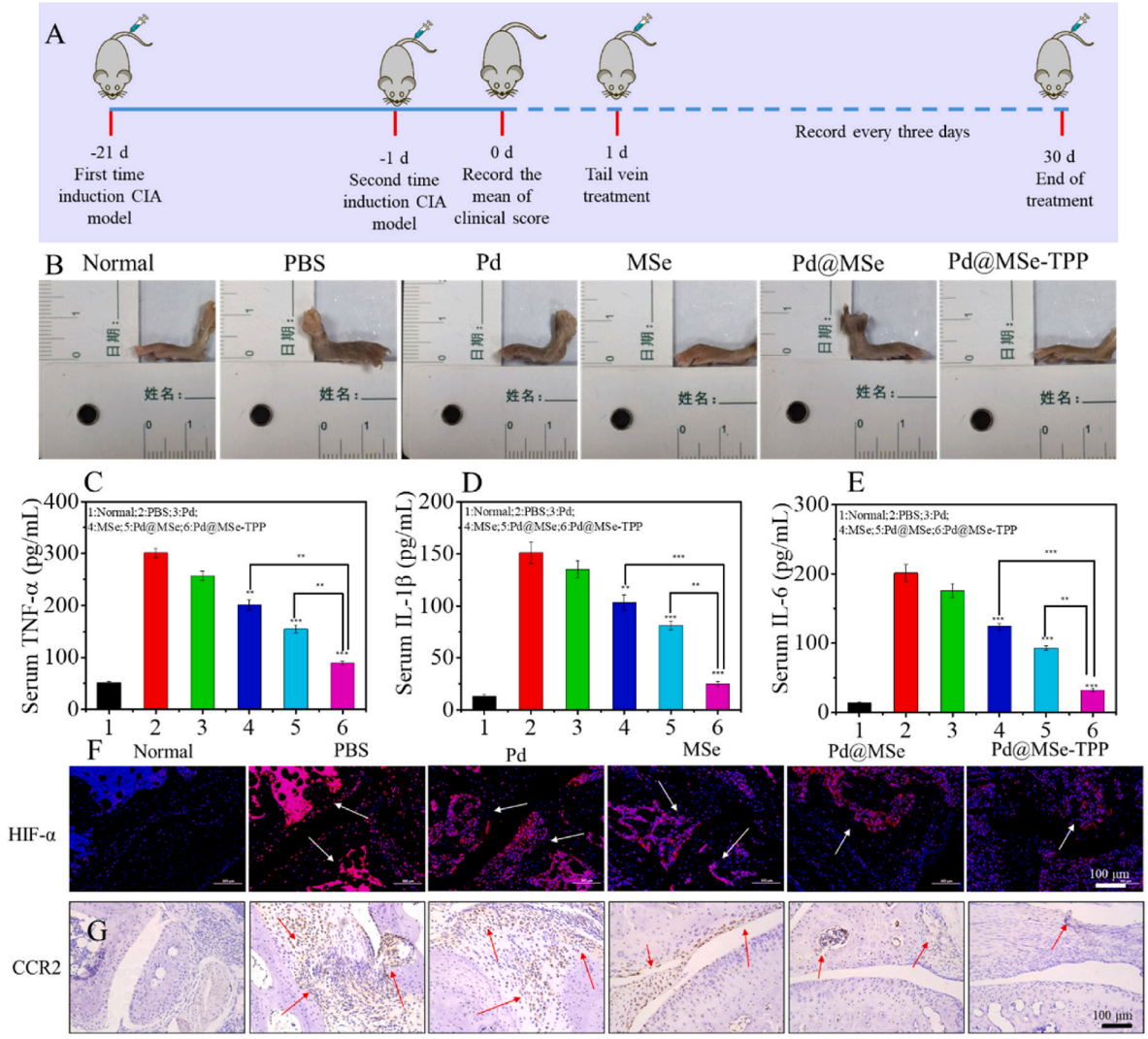

Fig. 8. In vivo regulates oxygen imbalance and inhibits inflammation. (A) The illustration of CIA model mice construction and treatment process. (B) The photographs of hind legs of mice taken on 30th day after various treatments. (C–E) The levels of pro-inflammatory cytokines (TNF-α, IL-1β and IL-6) on 30th day after various treatments by ELISA in peripheral blood. (F) The HIF-α expression in articular cartilage on 30th day after various treatments by immunofluorescence. (G) The CCR2 expression in articular cartilage on 30th day after various treatments by immunohistochemistry, (n = 5, mean ± SD, *p < 0.05, **p < 0.01, ***p < 0.001).

progression and spread of inflammation.

3.7. In vivo imaging and distribution of Pd@MSe-TPP nanomotors in CIA model mouse

Based on the previous experiments where Pd@MSe-TPP nanomotors demonstrated excellent diffusive motion and permeability through autonomous targeted driving, we further evaluated their distribution and penetration into joints in CIA model mice using an in vivo imaging system. First, we assessed the distribution of 40 μg/mL Cy5-labeled MSe nanozymes, Pd@MSe nanomotors, and Pd@MSe-TPP nanomotors in CIA mice at different time points following tail vein injection. As shown in Fig. 7A, due to the lack of autonomous diffusion and targeting capability, only a small amount of MSe nanozymes reached the lesion sites in CIA mice 2 h after injection. However, the Pd@MSe nanomotors, driven by autonomous motion, effectively diffused and penetrated into the joints of CIA mice. Notably, fluorescence from Pd@MSe nanomotors was observed at the lesion sites as early as 1 h post-injection, indicating effective entry into the affected areas. Nonetheless, the fluorescence intensity of Pd@MSe nanomotors in CIA joints did not increase over time. In contrast, Pd@MSe-TPP nanomotors, under the influence of dual driving forces, improved accumulation in the lesion sites of CIA mice through the targeting effect of TPP. This not only enabled effective diffusion and entry into the joints but also led to enhanced accumulation over time. Subsequent joint tissue sections provided clearer evidence that, at 2 h, the accumulation of Pd@MSe-TPP nanomotors in the mouse ankle joints was significantly higher than that of MSe nanozymes and Pd@MSe nanomotors (Fig. 7B), with fluorescence intensity reaching 1419, which is 2.8 times that of MSe nanozymes (Figure s16). Therefore, in vivo imaging further demonstrated that the construction of dual-driven Pd@MSe-TPP nanomotors not only effectively enhanced the diffusion of MSe nanozymes within mononuclear-macrophages but also improved their accumulation in the lesion areas of CIA model mice. Furthermore, to determine whether a concentration of 40 μg/mL Pd@MSe-TPP nanomotors is suitable for further in vivo studies, we conducted H&E pathological examinations of major organs to assess potential toxic side effects, along with toxicity evaluations for each group. As shown in Fig. 7C and Figure s17, after 24 h of administration, the same nanoparticles did not induce toxic side effects in the major organs, indicating good biocompatibility. This suggests that Pd@MSe-TPP nanomotors and their components are appropriate for in vivo studies.

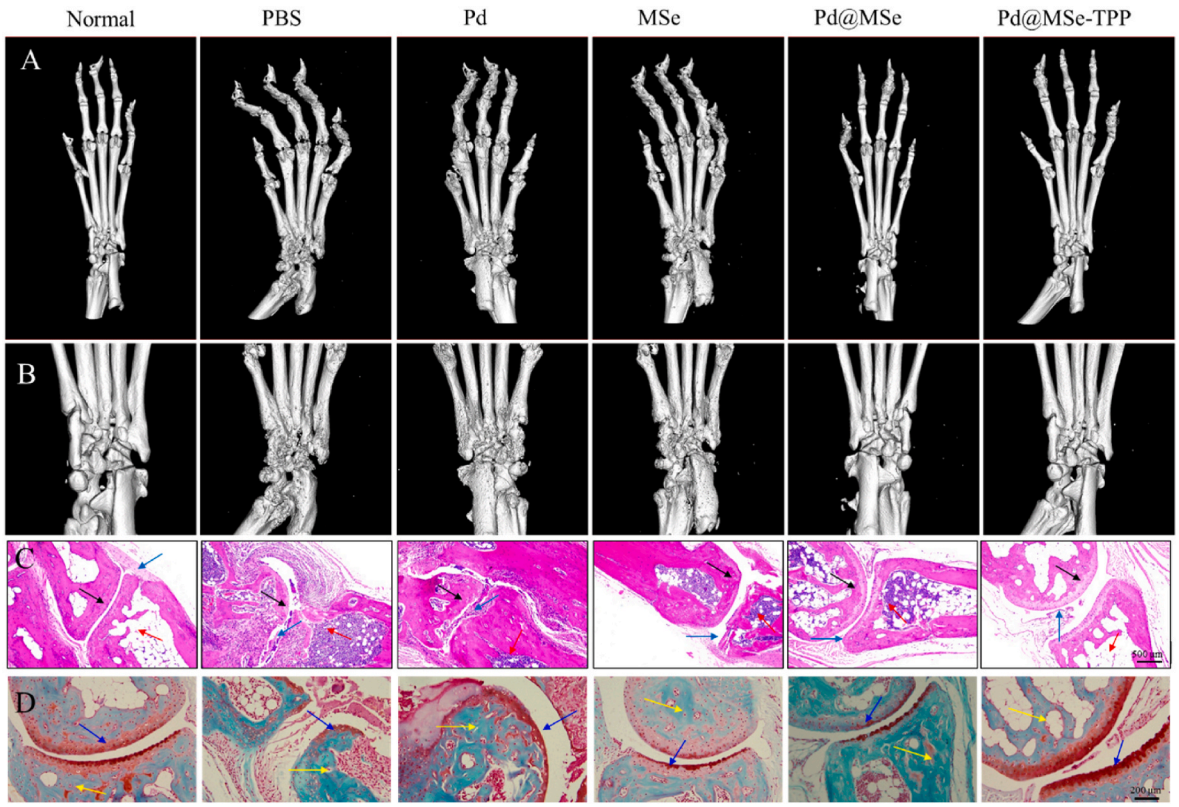

Fig. 9. The therapeutic effect of Pd@MSe-TPP nanomotors in inhibiting cartilage erosion. (A–B) The Micro-CT images of toe joints and ankle joints changes after various treatments. (C) The pathological sections of synovium and cartilage stained with H&E after various treatments. (D) The pathological sections of synovium and cartilage stained with Safranin O-Fast Green after various treatments(Saffranine O stains the cartilage, Fast Green stain bone tissue), (n = 5, mean ± SD).

3.8. The performances of nanomotors inhibits inflammation in vivo by regulating oxygen imbalance

The inflammatory response in RA plays a decisive role in immune regulation and changes in articular cartilage [57,58]. Therefore, to further evaluate the regulation of RA by Pd@MSe-TPP nanomotors, we first assessed the effectiveness of Pd@MSe-TPP nanomotors in suppressing the inflammatory response by modulating oxidative imbalance in CIA mice. We used male DBA/1 mice to establish the CIA model by injecting inducer with two immunizations over 21 days. Then we used the mean clinical scores to assess the severity of the inflammatory response in the CIA mice, and the end of the immune activation defined as day 0. Subsequently, the CIA mice were randomly divided into five groups (5 mice per group) and treated on day 1 with PBS, Pd nanozymes, MSe nanozymes, Pd@MSe nanomotors, and Pd@MSe-TPP nanomotors, respectively. Additionally, normal mice were used as a control group. The treatment groups received injections every two days, and the changes in clinical scores were recorded. On 30 days with a significant reduction of the mean clinical scores the mice were euthanized (Fig. 8A).

Initially, based on the changes in clinical scores, we observed that the CIA mice in the PBS group exhibited a persistent inflammatory response, leading to an increase in clinical scores over time, reaching a score of 16 at euthanasia on day 30 (Figure s18). This score indicated severe inflammation and limb swelling in the joints of the limbs, which was further confirmed by post-mortem images (Fig. 8B). In contrast, treatment with Pd nanozymes, MSe nanozymes, Pd@MSe nanomotors, and Pd@MSe-TPP nanomotors led to varying degrees of relief from hind limb swelling. Among these, Pd nanozymes had the least anti-inflammatory effect, as indicated by the relatively high clinical scores and severe joint swelling. The MSe nanozymes group showed noticeable redness and swelling, with clinical scores dropping to 8. The CIA mice treated with Pd@MSe nanomotors showed substantial improvement, with clinical scores dropping to 6, accompanied by only mild redness and swelling. The best results were observed in the group treated with Pd@MSe-TPP nanomotors, where the hind limbs exhibited no noticeable redness or swelling and clinical scores dropped to 3, approaching those of normal mice. These results suggest that Pd@MSe-TPP nanomotors effectively suppressed the inflammatory response in the limb joints of CIA mice. Subsequent analyses of peripheral blood for inflammatory cytokines (TNF-α, IL-1β, and IL-6), as well as the size of lymph nodes in the hind limbs, further revealed that treatment with Pd@MSe-TPP nanomotors significantly reduced pro-inflammatory cytokine levels (Fig. 8C–E), and prevented noticeable lymph node hyperplasia in the hind limbs (Figure s19). These findings indicate that Pd@MSe-TPP nanomotors not only suppress the inflammatory response but also reduce systemic chronic inflammation by blocking the inflammatory cascade. Additionally, histopathological analysis of the hind limbs across the different treatment groups confirmed these findings, showing that the expression of hypoxia-inducible factor HIF-α (Fig. 8F) and chemokine receptor CCR2 (Fig. 8G) in the joint cavities of CIA mice decreased to varying extents after varying treatment. Notably, treatment with Pd@MSe-TPP nanomotors brought these markers to levels close to those of normal mice, indicating that Pd@MSe-TPP nanomotors effectively ameliorated oxidative imbalance and inhibited chemotaxis, preventing the spread of the inflammatory response.

3.9. The therapeutic effect of Pd@MSe-TPP nanomotors in inhibiting cartilage erosion

Based on the articular cartilage as the final affected tissue in RA, it is also crucial to evaluate the progression of RA. Therefore, we further assessed the structural and pathological changes in the joints of mice in each group. Firstly, we utilized Micro-CT to observe the changes in the toe and ankle joints of mice in each group, as shown in Fig. 9A–B. In the

PBS group, under the severe erosion caused by the intense inflammatory cascade, the entire hind limb of the mice exhibited significant deformation, with nearly all toe joints showing marked erosion and degradation, and the ankle joints also suffering severe damage, resulting in a collapse of the entire structure. In contrast, the joint changes in the treatment groups were consistent with the expected trend in terms of the activity of the inflammatory response. Although the Pd nanozymes group showed some improvement in ankle joint degradation compared to the PBS group, all the toe joints still suffered severe damage. And the MSe nanozymes group, with a stronger ability to eliminate RONS, showed further improvement in joint degradation. The Pd@MSe nanomotors group demonstrated better therapeutic effects, with only partial joint degradation observed in CIA mice. Correspondingly, the Pd@MSe-TPP nanomotors group exhibited the best therapeutic effect, as the CT results not only revealed clear joint structures with only minor degradation in a few joints but also showed a bone surface-to-bone volume ratio approaching that of the normal group (Figure s20). These findings further confirm that the Pd@MSe-TPP nanomotors effectively protected the articular cartilage from inflammatory damage by regulating oxygen imbalance in RA. The histopathological analysis of H&E staining and Safranin O-Fast Green staining further corroborated these results. H&E staining clearly revealed severe cellular infiltration (red arrows), synovial hyperplasia (blue arrows), and bone tissue erosion (black arrows) in the joint cavity of CIA mice in the PBS group (Fig. 9C). Safranin O-Fast Green staining further demonstrated that the Safranin O staining was highly uneven in the PBS group (blue arrows), with only Fast Green staining visible (yellow arrows), indicating that the cartilage had almost completely degraded (Fig. 9D). However, after treatment with Pd nanozymes, MSe nanozymes, Pd@MSe nanomotors, and Pd@MSe-TPP nanomotors, varying degrees of improvement were observed, with the Pd@MSe-TPP nanomotors group showing only mild synovial hyperplasia and no cartilage erosion. Overall, the Pd@MSe-TPP nanomotors exhibit excellent in vivo and in vitro regulation of oxygen imbalance, anti-inflammatory effects, and inhibition of RA progression, providing an effective therapeutic strategy for treating RA.

4. Conclusion

Based on the oxygen imbalance in clinical RA patients, and the excessive RONS and oxygen deficiency in mononuclear macrophages are important causes of RAM oxygen imbalance, the regulation of oxygen imbalance is particularly critical for RA treatment. To achieve actively target the regulation oxygen imbalance in RAM and improve RA therapy, this study synthesis of an asymmetrically structured composite nanozyme motor (Pd@MSe-TPP nanomotors) that using endogenous H_2O_2 to generate oxygen and TPP forming a dual-drive power that allows the selenium nanozyme motors to autonomously diffuse into the mitochondria of monocytes-macrophages, and achieved synchronously inhibits excessive RONS and hypoxia. Following the rapid regulation of oxygen imbalance, Pd@MSe-TPP nanomotors not only effectively suppressed inflammatory response, but effectively blocking the inflammatory cascade reaction. Consequently, with the therapy of the Pd@MSe-TPP nanomotors, after restoring the oxygen balance, the spread of inflammation and the erosion of cartilage were significantly inhibited in CIA mice, thereby suppressing the progression of RA. This study provides significant scientific value and practical implications for reshaping RAM and improving RA treatment.

CRediT authorship contribution statement

Xu Chen: Writing – original draft, Investigation, Funding acquisition, Conceptualization. **Yang Yang:** Writing – review & editing, Methodology, Investigation. **Jiajun Chen:** Project administration, Investigation. **Yuebing He:** Methodology, Investigation. **Yukai Huang:** Project administration, Methodology. **Qidang Huang:** Supervision, Project administration. **Weiming Deng:** Supervision, Project administration. **Ruiqi Zhu:** Investigation. **Xuechan Huang:** Writing – review & editing, Investigation, Funding acquisition. **Tianwang Li:** Project administration, Methodology, Funding acquisition.

Declaration of competing interest

The authors declare that they have no known competing financial interests or personal relationships that could have appeared to influence the work reported in this paper.

Acknowledge

This work was supported by the National Natural Science Foundation of China (82201984,32301175), Natural Science Foundation of Guangdong Province(2024A1515013173), the Science Foundation of Guangdong Second Provincial General hospital (YY2022-007, 2024E007), the Guangdong Medical Research Foundation (A2023045), and the Fundamental and Applied Basic Research Project of Guangzhou City(2024A04J4810).

Appendix A. Supplementary data

Supplementary data to this article can be found online at https://doi.org/10.1016/j.redox.2025.103574.

Data availability

Data will be made available on request.

References

[1] A. Di Matteo, J.M. Bathon, P. Emery, Rheumatoid arthritis, Lancet 402 (10416) (2023) 2019–2033.
[2] S. Onuora, Rheumatic diseases on the rise, Nat. Rev. Rheumatol. 19 (7) (2023) 396, 396.
[3] Z.G. Li, A new look at rheumatology in China-opportunities and challenges, Nat. Rev. Rheumatol. 11 (5) (2015) 313–317.
[4] C.D. Buckley, C. Ospelt, S. Gay, K.S. Midwood, Location, location, location: how the tissue microenvironment affects inflammation in RA, Nat. Rev. Rheumatol. 17 (4) (2021) 195–212.
[5] M.M. Jeljeli, I.E. Adamopoulos, Innate immune memory in inflammatory arthritis, Nat. Rev. Rheumatol. 19 (10) (2023) 627–639.
[6] C.M. Weyand, J.J. Goronzy, Immunometabolism in early and late stages of rheumatoid arthritis, Nat. Rev. Rheumatol. 13 (5) (2017) 1–11.
[7] M.H. Smith, J.R. Berman, What is rheumatoid arthritis? JAMA 327 (12) (2022) 1194.
[8] C.T. Ng, M. Biniecka, A. Kennedy, J. McCormick, O. FitzGerald, B. Bresnihan, D. Buggy, C.T. Taylor, J. O'Sullivan, U. Fearon, D.J. Veale, Synovial tissue hypoxia and inflammation in vivo, Ann.Rheu.Dis. 69 (7) (2010) 1389–1395.
[9] Y.L.C. Becker, B. Duvvuri, P.R. Fortin, C. Lood, E. Boilard, The role of mitochondria in rheumatic diseases, Nat. Rev. Rheumatol. 18 (11) (2022) 621–640.
[10] Y. Zhu, T.J. Zhao, M. Liu, S.Y. Wang, S.L. Liu, Y.R. Yang, Y.Q. Yang, Y.Y. Nan, Q. Huang, K.L. Ai, Rheumatoid arthritis microenvironment insights into treatment effect of nanomaterials, Nano Today 42 (2022) 101358.
[11] J. Kim, H.Y. Kim, S.Y. Song, S.H. Go, H.S. Sohn, S. Baik, M. Soh, K. Kim, D. Kim, H. C. Kim, N. Lee, B.S. Kim, T. Hyeon, Synergistic oxygen generation and reactive oxygen species scavenging by manganese ferrite/ceria Co-decorated nanoparticles for rheumatoid arthritis treatment, ACS Nano 13 (3) (2019) 3206–3217.
[12] R.R. Ni, G.J. Song, X.H. Fu, R.F. Song, L.L. Li, W.D. Pu, J.N. Gao, J. Hu, Q. Liu, F. T. He, D.L. Zhang, G. Huang, Reactive oxygen species-responsive dexamethasone-loaded nanoparticles for targeted treatment of rheumatoid arthritis via suppressing the iRhom2/TNF-α/BAFF signaling pathway, Biomaterials 232 (2020) 119730.
[13] L.Z. Gao, H. Wei, S.J. Dong, X.Y. Yan, The nanozymes, Adv. Mater. 36 (10) (2024) 2305249.
[14] H.Z. Fan, R.F. Zhang, K.L. Fan, L.Z. Gao, X.Y. Yan, Exploring the specificity of nanozymes, ACS Nano 18 (4) (2024) 2533–2540.
[15] M.Y. Li, H. Jiang, P. Hu, J.L. Shi, Nanocatalytic anti-tumor immune regulation, Angew.Chem.Int. Edit. 63 (13) (2024), https://doi.org/10.1002/anie.202316606.
[16] X.Y. Lu, S.S. Gao, H. Lin, L.D. Yu, Y.H. Han, P.A. Zhu, W.C. Bao, H.L. Yao, Y. Chen, J.L. Shi, Bioinspired copper single-atom catalysts for tumor parallel catalytic therapy, Adv. Mater. 32 (36) (2020) 2002246.
[17] B.W. Yang, H.L. Yao, J.C. Yang, C. Chen, Y.D. Guo, H. Fu, J.L. Shi, In situ synthesis of natural antioxidase mimics for catalytic anti-inflammatory treatments: rheumatoid arthritis as an example, J.Am. Chem. Soc. 144 (1) (2022) 314–330.
[18] L. Zhang, H. Wang, X.G. Qu, Biosystem-inspired engineering of nanozymes for biomedical applications, Adv. Mater. 36 (10) (2024), https://doi.org/10.1002/adma.202211147.

[19] F. Muhammad, F.T. Huang, Y. Cheng, X.W. Chen, Q. Wang, C.X. Zhu, Y.H. Zhang, X.H. Yang, P. Wang, H. Wei, Nanoceria as an electron reservoir: spontaneous deposition of metal nanoparticles on oxides and their anti-inflammatory activities, ACS Nano 16 (12) (2022) 20567–20576.
[20] C.B. Ma, Y.P. Xu, L.X. Wu, Q. Wang, J.J. Zheng, G.X. Ren, X.Y. Wang, X.F. Gao, M. Zhou, M. Wang, H. Wei, Guided synthesis of a Mo/Zn dual single-atom nanozyme with synergistic effect and peroxidase-like activity, Angew.Chem.Int. Edit. (2022) e202116170.
[21] S. Ghosh, P. Roy, N. Karmodak, E.D. Jemmis, G. Mugesh, Nanoisozymes: crystal-facet-dependent enzyme-mimetic activity of V2O5 nanomaterials, Angew.Chem. Int. Edit. 57 (17) (2018) 4510–4515.
[22] N. Singh, G.R. Sherin, G. Mugesh, Antioxidant and prooxidant nanozymes: from cellular redox regulation to next-generation therapeutics, Angew.Chem.Int. Edit. 62 (33) (2023), https://doi.org/10.1002/anie.202301232.
[23] Y. Zhang, T.T. Cui, J. Yang, Y. Huang, J.S. Ren, X.G. Qu, Chirality-dependent reprogramming of macrophages by chiral nanozymes, Angew.Chem.Int. Edit. 62 (34) (2023), https://doi.org/10.1002/anie.202307076.
[24] J.J.X. Wu, Y.J. Yu, Y. Cheng, C.Q. Cheng, Y.H. Zhang, B. Jiang, X.Z. Zhao, L. Y. Miao, H. Wei, Ligand-dependent activity engineering of glutathione peroxidase-mimicking MIL-47(V) metal-organic framework nanozyme for therapy, Angew. Chem.Int. Edit. 60 (3) (2021) 1227–1234.
[25] C.F. Wei, Y.A. Liu, X.F. Zhu, X. Chen, Y.H. Zhou, G.L. Yuan, Y.C. Gong, J. Liu, Iridium/ruthenium nanozyme reactors with cascade catalytic ability for synergistic oxidation therapy and starvation therapy in the treatment of breast cancer, Biomaterials 238 (2020) 119848.
[26] X. Chen, Z. Jia, Y.Y. Wen, Y.Q. Huang, X.Y. Yuan, Y.T. Chen, Y.A. Liu, J. Liu, Bidirectional anisotropic palladium nanozymes reprogram macrophages to enhance collaborative chemodynamic therapy of colorectal cancer, Acta Biomater. 151 (2022) 537–548.
[27] J.C. Avery, P.R. Hoffmann, Selenium, selenoproteins, and immunity, Nutrients 10 (9) (2018) 1203.
[28] J. Ouyang, B. Deng, B.H. Zou, Y.J. Li, Q.Y. Bu, Y. Tian, M.K. Chen, W. Chen, N. Kong, T.F. Chen, W. Tao, Oral hydrogel microbeads-mediated in situ synthesis of selenoproteins for regulating intestinal immunity and microbiota, J.Am. Chem. Soc. 145 (22) (2023) 12193–12205.
[29] L.J. Huang, X.T. Mao, Y.Y. Li, D.D. Liu, K.Q. Fan, R.B. Liu, T.T. Wu, H.L. Wang, Y. Zhang, B. Yang, C.Q. Ye, J.Y. Zhong, R.J. Chai, Q. Cao, J. Jin, Multiomics analyses reveal a critical role of selenium in controlling T cell differentiation in Crohn's disease, Immunity 54 (8) (2021) 1728–+.
[30] F. Li, T.Y. Li, C.X. Sun, J.H. Xia, Y. Jiao, H.P. Xu, Selenium-doped carbon quantum dots for free-radical scavenging, Angew.Chem.Int. Edit. 56 (33) (2017) 9910–9914.
[31] H.Q. Lai, L.G. Xu, C. Liu, S.J. Shi, Y.L. Jiang, Y.Y. Yu, B. Deng, T.F. Chen, Universal selenium nanoadjuvant with immunopotentiating and redox-shaping activities inducing high-quality immunity for SARS-CoV-2 vaccine, Signal Transduct. Target 8 (1) (2023) 88.
[32] B.H. Zou, Z.S. Xiong, Y.Z. Yu, S.J. Shi, X.L. Li, T.F. Chen, Rapid selenoprotein activation by selenium nanoparticles to suppresses osteoclastogenesis and pathological bone loss, Adv.Mater. 36 (27) (2024), https://doi.org/10.1002/adma.202401620.
[33] Z.S. Xiong, H. Lin, H. Li, B.H. Zou, B. Xie, Y.Z. Yu, L.Z. He, T.F. Chen, Chiral selenium nanotherapeutics regulates selenoproteins to attenuate glucocorticoid-induced osteoporosis, Adv. Funct. Mater. 33 (17) (2023), https://doi.org/10.1002/adfm.202212970.
[34] C.P. Zheng, J.S. Wang, Y.N. Liu, Q.Q. Yu, Y. Liu, N. Deng, J. Liu, Functional selenium nanoparticles enhanced stem cell osteoblastic differentiation through BMP signaling pathways, Adv. Funct. Mater. 24 (43) (2014) 6872–6883.
[35] J. Sun, C.F. Wei, Y.A. Liu, W.J. Xie, M.M. Xu, H. Zhou, J. Liu, Progressive release of mesoporous nano-selenium delivery system for the multi-channel synergistic treatment of Alzheimer's disease, Biomaterials 197 (2019) 417–431.
[36] A.G. Lin, Y.A. Liu, X.F. Zhu, X. Chen, J.W. Liu, Y.H. Zhou, X.Y. Qin, J. Liu, Bacteria-Responsive biomimetic selenium nanosystem for multidrug-resistant bacterial infection detection and inhibition, ACS Nano 13 (12) (2019) 13965–13984.
[37] X. Chen, X.F. Zhu, Y.C. Gong, G.L. Yuan, J.Q. Cen, Q.S. Lie, Y.D. Hou, G. Ye, S. M. Liu, J. Liu, Porous selenium nanozymes targeted scavenging ROS synchronize therapy local inflammation and sepsis injury, App. Mater. Today 22 (2021) 100929.
[38] C.P. Zheng, A.P. Wu, X.Y. Zhai, H. Ji, Z.K. Chen, X. Chen, X.Y. Yu, The cellular immunotherapy of integrated photothermal anti-oxidation Pd-Se nanoparticles in inhibition of the macrophage inflammatory response in rheumatoid arthritis, Acta Pharm. Sin. B 11 (7) (2021) 1993–2003.
[39] Y.C. Gong, A.L. Huang, X. Guo, Z. Jia, X. Chen, X.F. Zhu, Y. Xia, J. Liu, Y. Xu, X. Y. Qin, Selenium-core nanozymes dynamically regulates Aβ & neuroinflammation circulation: augmenting repair of nervous damage, Chem. Eng. J. 418 (2021) 129345.
[40] X. Chen, Y.L. Yang, Q.M. Mai, G. Ye, Y.N. Liu, J. Liu, Pillar arene Se nanozyme therapeutic systems with dual drive power effectively penetrated mucus layer combined therapy acute lung injury, Biomaterials 304 (2024) 122384.
[41] A. Somasundar, S. Ghosh, F. Mohajerani, L.N. Massenburg, T.L. Yang, P.S. Cremer, D. Velegol, A. Sen, Positive and negative chemotaxis of enzyme-coated liposome motors, Nat. Nanotechnol. 14 (12) (2019), 1129-+.
[42] H.Y. Zhang, Z.S. Li, C.Y. Gao, X.J. Fan, Y.X. Pang, T.L. Li, Z.G. Wu, H. Xie, Q. He, Dual-responsive biohybrid neutrobots for active target delivery, Sci. Robot. 6 (52) (2021) eaaz9519.
[43] Z.Y. Wu, L. Chen, W.Y. Guo, J. Wang, H.Y. Ni, J.N. Liu, W.T. Jiang, J. Shen, C. Mao, M. Zhou, M.M. Wan, Oral mitochondrial transplantation using nanomotors to treat ischaemic heart disease, Nat. Nanotechnol. (2024), https://doi.org/10.1038/s41565-024-01681-7.
[44] H. Chen, T. Li, Z.Y. Liu, S.W. Tang, J.T. Tong, Y.F. Tao, Z.N. Zhao, N. Li, C. Mao, J. Shen, M.M. Wan, A nitric-oxide driven chemotactic nanomotor for enhanced immunotherapy of glioblastoma, Nat. Comm. 14 (1) (2023).
[45] H. Chen, T. Shi, Y. Wang, Z.Y. Liu, F.C. Liu, H.Y. Zhang, X.W. Wang, Z.Y. Miao, B. R. Liu, M.M. Wan, C. Mao, J. Wei, Deep penetration of nanolevel drugs and micrometer-level T cells promoted by nanomotors for cancer immunochemotherapy, J.Am. Chem. Soc. 143 (31) (2021) 12025–12037.
[46] T. Li, Z.Y. Liu, J.L. Hu, L. Chen, T.T. Chen, Q.Q. Tang, B.X. Yu, B. Zhao, C. Mao, M. M. Wan, A universal chemotactic targeted delivery strategy for inflammatory diseases, Adv. Mater. 35 (31) (2023) 202206654.
[47] M.L. Liu, L. Chen, Z.W. Zhao, M.C. Liu, T.C. Zhao, Y.Z. Ma, Q.Y. Zhou, Y.S. Ibrahim, A.A. Elzatahry, X.M. Li, D.Y. Zhao, Enzyme-based mesoporous nanomotors with near-infrared optical brakes, J.Am. Chem. Soc. 144 (9) (2022) 3892–3901.
[48] C. Xu, Y.J. Jiang, H. Wang, Y.X. Zhang, Y.C. Ye, H.F. Qin, J.B. Gao, Q. Dan, L.L. Du, L. Liu, F. Peng, Y.J. Li, Y.F. Tu, Arthritic microenvironment actuated nanomotors for active rheumatoid arthritis therapy, Adv. Sci. 10 (4) (2023) 2204881.
[49] M.L. Lian, Z.J. Xue, X.Z. Qiao, C. Liu, S. Zhang, X. Li, C.H. Huang, Q. Song, W. S. Yang, X. Chen, T. Wang, Movable hollow nanoparticles as reactive oxygen scavengers, Chem 5 (9) (2019) 2378–2387.
[50] J.W. Sun, M. Mathesh, W. Li, D.A. Wilson, Enzyme-powered nanomotors with controlled size for biomedical applications, ACS Nano 13 (9) (2019) 10191–10200.
[51] J.R. Howse, R.A. Jones, A.J. Ryan, T. Gough, R. Vafabakhsh, R.J. P.r. l. Golestanian, Self-motile colloidal particles: from directed propulsion to random walk, Phys. Rev. Lett. 99 (4) (2007) 048102.
[52] L.H. Wang, R. Luqmani, I.A. Udalova, The role of neutrophils in rheumatic disease-associated vascular inflammation, Nat. Rev. Rheumatol. 18 (3) (2022) 158–170.
([53])Z.X. Tu, Y.L. Zhong, H.Z. Hu, D. Shao, R.N. Haag, M. Schirner, J. Lee, B. Sullenger, K.W. Leong, Design of therapeutic biomaterials to control inflammation, Nat. Rev. Mater. 7 (7) (2022) 557–574.
[54] S. Victorelli, H. Salmonowicz, J. Chapman, H. Martini, M.G. Vizioli, J.S. Riley, C. Cloix, E. Hall-Younger, J.M. Espindola-Netto, D. Jurk, A.B. Lagnado, L.S. Gomez, J.N. Farr, D. Saul, R. Reed, G. Kelly, M. Eppard, L.C. Greaves, Z.X. Dou, N. Pirius, K. Szczepanowska, R.A. Porritt, H.J. Huang, T.Y. Huang, D.A. Mann, C.A. Masuda, S. Khosla, H.M. Dai, S.H. Kaufmann, E. Zacharioudakis, E. Gavathiotis, N. K. LeBrasseur, X. Lei, A.G. Sainz, V.I. Korolchuk, P.D. Adams, G.S. Shadel, S.W. G. Tait, J.F. Passos, Apoptotic stress causes mtDNA release during senescence and drives the SASP, Nature 622 (7983) (2023) 627.
[55] L. Li, J.S. Cao, S. Li, T.Y. Cui, J.Y. Ni, H. Zhang, Y. Zhu, J.Y. Mao, X.M. Gao, A. C. Midgley, M.F. Zhu, G.W. Fan, M2 macrophage-derived sEV regulate pro-inflammatory CCR2+ macrophage subpopulations to favor post-AMI cardiac repair, Adv. Sci. 10 (14) (2023).
[56] C.M. Weyand, J.J. J.N.i. Goronzy, The immunology of rheumatoid arthritis, Nat. Immunol. 22 (1) (2021) 10–18.
[57] H. Li, G.C. Tsokos, IL-23/IL-17 Axis in inflammatory rheumatic diseases, Clin. Rev. Allerg. Immu. 60 (1) (2021) 31–45.
[58] I. Cambré, D. Gaublomme, A. Burssens, P. Jacques, N. Schryvers, A. De Muynck, L. Meuris, S. Lambrecht, S. Carter, P. de Bleser, Y. Saeys, L. Van Hoorebeke, G. Kollias, M. Mack, P. Simoens, R. Lories, N. Callewaert, G. Schett, D. Elewaut, Mechanical strain determines the site-specific localization of inflammation and tissue damage in arthritis, Nat. Comm. 9 (2018) 4613.